A large-eddy-simulation-based numerical wave tank for three-dimensional wave-structure interaction

Aristos Christou[a], Thorsten Stoesser[a,*], Zhihua Xie[b]

[a]*Department of Civil, Environmental and Geomatic Engineering, University College London, Gower Street, WC1E 6BT, London, UK*
[b]*School of Engineering, Cardiff University, Cardiff, CF24 3AA, UK*

Abstract

A three-dimensional numerical wave tank (NWT) based on the large eddy simulation (LES) code Hydro3D is introduced. The open-source code employs the level set and immersed boundary methods in order to compute the water surface and to account for solid structures in the numerical tank, respectively. The spatially-filtered Navier-Stokes (N-S) equations are solved on a staggered Cartesian grid using the finite difference method while time advancement is achieved using the fractional-step method based on a three-step Runge-Kutta scheme. Velocities and pressure are coupled with the Poisson equation and its solution is obtained via a multi-grid technique. The NWT is then applied to predict the progression and damping of monochromatic waves and the interaction of non-linear waves with various submerged obstacles. The accuracy of the NWT is confirmed by comparing numerical results with data of previously reported laboratory experiments. Comparisons of numerically predicted and measured water-level elevations, local velocity and pressure fields and forces acting on structures under the influence of incoming waves agree well and confirm that the LES-based NWT is able to predict accurately three-dimensional wave-structure interaction.

Keywords: Numerical wave tank, LES, non-linear waves, Wave-structure interaction, Turbulence, level set method, immersed boundary method

1. Introduction

The need for improved coastal protection as well as the continuous exploitation of offshore energy resources require improved designs of coastal and offshore structures to ensure their long-term functionality and durability under more frequently recurring extreme wave conditions. Many experimental studies have investigated and confirmed the existence of complex wave-structure interactions over a wide range and variety of offshore-engineering applications [1–3]. Complementary to experimentally-based research a large number of numerical models have been developed to investigate such problems producing accurate results for a wide range of applications.

---

*Corresponding author
Email address: t.stoesser@ucl.ac.uk (Thorsten Stoesser)

Potential flow theory (PFT) has been extensively used for the development of numerical wave tanks
(NWTs) with the goal to model the progression and interaction of water waves with offshore structures. PFT-based models are efficient for studying coastal engineering applications and are currently widely used. For instance, in [4] the 3D Laplace equation was solved using a harmonic polynomial cell (HPC) method whereas [5] adopted a splitting technique to decompose the variables into an incident and scatter component. Based on Boundary Integral Equations Methods (BIEM) [6], [7] carried out simulations of waves interacting with a square step and the results are compared with experimental data obtained in the same study. Alternatively, [8, 9] calculated the forces acting on a submerged structure considering solitary and cnoidal waves based on fluid sheets originally developed by [10] assuming an inviscid and incompressible fluid. However, the reliability of such models to simulate complex wave-structure interaction (WSI) problems, especially when wave breaking occurs or complex turbulent flow structures exist, is limited by the code's primary assumptions.

Due to the increase in computational resources, models which solve the Navier-Stokes equations, known as Computational Fluid Dynamics (CFD), employed as a NWT have become popular recently. According to the CFD method's solution approach, these can be categorized in Direct Numerical Simulations (DNS), Reynolds Averaged Navier-Stokes (RANS), Large eddy Simulations (LES), or a hybrid of the latter two, Detached Eddy Simulations (DES). DNS produces the most accurate results however its application to practical problems is limited due to its extremely high computational cost. In LES, large flow structures are simulated directly while small-, dissipative-scale structures, smaller than the grid size, are modelled based by sub-grid scale (SGS) models to enable energy dissipation from the directly-resolved large scales. The most common SGS models are the Smagorinsky model [11] and the Wall-Adapting Local Eddy viscosity (WALE) SGS model [12]. In the latter one, wall effects are intrinsically considered and the resolved velocity-gradient is adopted to calculate the eddy viscosity near the boundary. In contrast, in Smagorinsky's model, the near-wall subgrid-scale eddy viscosity requires modification using a wall-damping function. A review of LES and its applications can be found in [13]. The technique adopted to track or capture the interface between two phases (e.g. water and air in free-surface flows) can further be used to classify CFD methods. The most common free-surface models are the Level-Set Method (LSM) [14] and Volume of Fluid (VoF) [15]. In the latter, a fractional volume is defined to distinguish cells between phases whereas in LSM a level set signed distance function is employed to define the interface between the two phases. The VOF method produces better results in terms of mass and volume conservation whereas higher order schemes such as Weighted Essentially Non-Oscillatory (WENO) schemes [16] can be used in LSM and also produce smoother curvatures of the interface [17, 18].

In the literature, several numerical models exist based on the above methods. For example, [19, 20] employed NWT toolboxes in the open-source code, OpenFOAM that capture the free-surface using the VOF method.In OpenFOAM the user can employ various approaches to solve the N-S equations for example RANS or LES, however, in the above studies RANS models were adopted. In [19], waves are generated in the numerical tank based on theoretical solutions of the free-surface and particles velocities, while an active

wave absorption method, similar to physical flumes, is employed to absorb waves at any boundary. The same authors, recently developed a new wave generation method using moving boundaries in [21]. Based on the same open-source code, [20] generate and absorb waves using the relaxation technique [22] where computed values of the water surface and velocity components are gradually set to a desired value inside a relaxation zone near the inlet or outlet of the domain. Alternatively, [23] developed a three-dimensional NWT employing LES, VOF and cut-cell method [24] to simulate complex 3D WSI problems in which waves are generated in the tank based on theoretical solutions of the wave-elevation and velocity components. RANS modelling was employed by [25] to develop a NWT, known as REEF3D [26], that captures the free-surface using LSM among with a ghost cell immersed boundary method [27] to generate complex solid geometries. Similarly, [28, 29] proposed a new NWT using Fast Direct Solvers (FDS) for the solution of the Poisson equation and the LSM for free-surface tracking. In the same study, a modified ghost-cell BM is presented to generate solid structures in the tank in an LES numerical framework.

In the study reported here, the LES code Hydro3D is further refined to develop a 3D NWT, referred to hereafter as Hydro3D-NWT. It is based on the method of large eddy simulation and includes the level-set and immersed boundary methods and employed for the simulation of three-dimensional wave-structure interaction. The novelty of Hydro3D-NWT arises from the adoption of the efficient IBM proposed in [30], a quick active wave generation, LSM for capturing the water surface and the employment of a wall-adaptive SGS model in LES to simulate three-dimensional two-phase simulations, which are different from previous LES studies [29, 31]. While the above numerical methods have all been employed to study various wave interaction problems, the combination of these (i.e. IBM, LSM and WALE SGS model) applied in NWTs with complex wave-structure-interactions has not been considered yet. The open-source code Hydro3D-NWT is developed to allow application to complex three-dimensional geometries with the goal to enhance the knowledge and understanding of the physics and flow development as well structural analysis of complex 3D WSI problems. The objective of the study is to demonstrate Hydro3D-NWT's accuracy and efficiency in predicting complex three-dimensional wave-structure interaction. Section 2 presents the numerical framework of the code together with two benchmark cases of a solitary wave propagating in a tank and the generation, progression and absorption of periodic non-linear waves. The performance of the code is further examined in Section 3 where simulations of previous laboratory experiments are re-constructed and hydrodynamic properties and wave-elevations are compared with experimental measurements. Finally, main conclusion and future work are discussed in Section 4.

2. Numerical Framework

Hydro3D is an open-source code [32], validated recently in several engineering applications [33–35] and is refined for a NWT [36] enabling the simulation of wave-structure interaction (WSI). The code is parallelised and the computational domain is decomposed into multiple sub-domains and the message-passing interface (MPI) exchanges information between different subdomains/processors [37]. In the following a detailed

description of the numerical framework of Hydro3D-NWT is provided.

2.1. Flow solver

Hydro3D-NWT solves the unsteady, incompressible, viscous spatially-filtered Navier-Stokes equations, written in tensor notation:

$$\frac{\partial \bar{u}_i}{\partial x_i} = 0 \tag{1}$$

$$\frac{\partial \bar{u}_i}{\partial t} + \frac{\partial \bar{u}_i \bar{u}_j}{\partial x_j} = -\frac{1}{\rho}\frac{\partial \bar{p}}{\partial x_i} + \frac{\partial}{\partial x_j}\left(\nu\frac{\partial \bar{u}_i}{\partial x_j}\right) - \frac{\partial \tau_{ij}^{SGS}}{\partial x_j} + f_i + g_i \tag{2}$$

where $\bar{u}_i$ is the instantaneous filter velocity in the x_i direction and $\bar{p}$ the pressure field. ρ and ν are the fluid density and kinematic viscosity, respectively and τ_{ij}^{SGS} the sub-grid scale (SGS) stress tensor. f_i is the forcing term of the immersed boundary method acting on the fluid and g_i the gravitational acceleration.

2.1.1. SGS model

In LES a subgrid-scale (SGS) model is required to remove energy from the large scales of the flow. The SGS model emulates the effects of the small scales on the large scales by employment of the Boussinesq approximation, similar to the concept of RANS turbulence modeling, i.e. via an eddy viscosity ν_t. Hydro3D-NWT employs the Wall-Adapting Local Eddy viscosity (WALE) model [12] which uses the information from the resolved velocity tensor $\bar{g}_{ij} = \dfrac{\partial \bar{u}_i}{\partial x_j}$ to calculate ν_t as:

$$\nu_t = (C_w\Delta)^2 \frac{(S_{ij}^d S_{ij}^d)^{3/2}}{(\bar{S}_{ij}\bar{S}_{ij})^{5/2} + (S_{ij}^d S_{ij}^d)^{5/4}} \tag{3}$$

where C_w is an empirical constant set to $C_w = 0.46$ and the size of the filter width is calculated as $\Delta = (dx \cdot dy \cdot dz)^{1/3}$.

$$\bar{S}_{ij} = \frac{1}{2}\left(\frac{\partial \bar{u}_i}{\partial x_j} + \frac{\partial \bar{u}_j}{\partial x_i}\right) \tag{4}$$

is the deformation tensor of the resolved field and the traceless symmetric part of the velocity tensor S_{ij}^d defined as:

$$S_{ij}^d = \frac{1}{2}(\bar{g}_{ij}^2 + \bar{g}_{ji}^2) - \frac{1}{3}\delta_{ij}\bar{g}_{kk}^2 \tag{5}$$

where δ_{ij} is the Kronecker symbol and $\bar{g}_{ij}^2 = \bar{g}_{ik}\bar{g}_{kj}$. The total viscosity ν_T is the sum of molecular and eddy viscosity, i.e. $\nu_T = \nu + \nu_t$. The main advantage of the WALE model is that the eddy viscosity is computed to be negligibly small inside a viscous layer near walls and hence it does not require an additional wall damping function as for example the standard Smagorinsky model [11].

2.1.2. Domain discretization

Equations (1) and (2) are discretized with the finite difference method on a staggered uniform Cartesian grid. In staggered grids, Fig. 1a, scalar quantities are calculated at the centre of the cell while velocities and their derivatives are calculated at the cells' faces. For simplicity, the following equations are expanded only in two dimensions. Using the finite difference method, the momentum equation (Eq. (2)) is divided into convective and diffusive terms as follows:

$$Convective\ terms: \frac{\partial \bar{u}_i \bar{u}_j}{\partial x_j} \tag{6}$$

$$Diffusive\ terms: \frac{\partial}{\partial x_j}\left(\nu_T \frac{\partial \bar{u}_i}{\partial x_j}\right) \tag{7}$$

where the spatial partial derivatives of the convective term are calculated using 4th order central differences (CDS) while diffusive terms are discretized using 2nd order CDS. 4th order CDS is used for the convective terms rather than UPWIND or blended schemes to avoid numerical dissipation and maintain high-order accuracy. For example, the convective terms in Eq. (6) are approximated in the X-direction at the east face as:

$$
\begin{aligned}
\frac{\partial \bar{u}_i \bar{u}_j}{\partial x_j} = \frac{\partial \bar{u}\bar{u}}{\partial x} + \frac{\partial \bar{u}\bar{w}}{\partial z} &= \frac{-\bar{u}_p^2(i+2,k) + 27\bar{u}_p^2(i+1,k) - 27\bar{u}_p^2(i,k) + \bar{u}_p^2(i-1,k)}{24dx} \\
&+ \frac{-\bar{u}_c(i,k+1)\bar{w}_c(i,k+1) + 27\bar{u}_c(i,k)\bar{w}_c(i,k) - 27\bar{u}_c(i,k-1)\bar{w}_c(i,k-1) + \bar{u}_c(i,k-2)\bar{w}_c(i,k-2)}{24dz}
\end{aligned}
\tag{8}
$$

and in Z-direction at the cell's top face:

$$
\begin{aligned}
\frac{\partial \bar{u}_i \bar{u}_j}{\partial x_j} = \frac{\partial \bar{w}\bar{w}}{\partial z} + \frac{\partial \bar{u}\bar{w}}{\partial x} &= \frac{-\bar{w}_p^2(i,k+2) + 27\bar{w}_p^2(i,k+1) - 27\bar{w}_p^2(i,k) + \bar{w}_p^2(i,k-1)}{24dz} \\
&+ \frac{-\bar{u}_c(i+1,k)\bar{w}_c(i+1,k) + 27\bar{u}_c(i,k)\bar{w}_c(i,k) - 27\bar{u}_c(i-1,k)\bar{w}_c(i-1,k) + \bar{u}_c(i-2,k)\bar{w}_c(i-2,k)}{24dx}
\end{aligned}
\tag{9}
$$

using the interpolated values of the velocities at the centre $\tilde{u}_{i_p}$ or the corner of the cell $\tilde{u}_{i_c}$ for the cross term uw (see Fig. 1a for the location of interpolated velocities):

$$
\begin{aligned}
\bar{u}_p(i,k) &= \frac{1}{16}(-\bar{u}(i-2,k) + 9\bar{u}(i-1,k) + 9\bar{u}(i,k) - \bar{u}(i+1,k)) \\
\bar{w}_p(i,k) &= \frac{1}{16}(-\bar{w}(i,k-2) + 9\bar{w}(i,k-1) + 9\bar{w}(i,k) - \bar{w}(i,k+1)) \\
\bar{u}_c(i,k) &= \frac{1}{16}(-\bar{u}(i,k-1) + 9\bar{u}(i,k) + 9\bar{u}(i,k+1) - \bar{u}(i,k+2)) \\
\bar{w}_c(i,k) &= \frac{1}{16}(-\bar{w}(i-1,k) + 9\bar{u}(i,k) + 9\bar{u}(i+1,k) - \bar{u}(i+2,k))
\end{aligned}
\tag{10}
$$

Diffusive terms in Eq. (7) are approximated in the X-direction as::

$$
\begin{aligned}
\frac{\partial}{\partial x_j}\left(\nu_T \frac{\partial \bar{u}_i}{\partial x_j}\right) = \nu_T\left(\frac{\partial^2 \bar{u}}{\partial x^2} + \frac{\partial^2 \bar{u}}{\partial z^2}\right) &= \nu_T\left(\frac{\bar{u}(i+1,k) - 2\bar{u}(i,k) + \bar{u}(i-1,k)}{dx^2}\right) \\
&+ \nu_T\left(\frac{\bar{u}(i,k+1) - 2\bar{u}(i,k) + \bar{u}(i,k-1)}{dz^2}\right)
\end{aligned}
\tag{11}
$$

5

and in Z-direction as:

$$\frac{\partial}{\partial x_j}\left(\nu_T \frac{\partial \bar{u}_i}{\partial x_j}\right) = \nu_T\left(\frac{\partial^2 \bar{w}}{\partial x^2} + \frac{\partial^2 \bar{w}}{\partial z^2}\right) = \nu_T\left(\frac{\bar{w}(i+1,k) - 2\bar{w}(i,k) + \bar{w}(i-1,k)}{dx^2}\right)$$
$$+\nu_T\left(\frac{\bar{w}(i,k+1) - 2\bar{w}(i,k) + \bar{w}(i,k-1)}{dz^2}\right) \tag{12}$$

(a) Staggered grid

(b) 2D grid representation
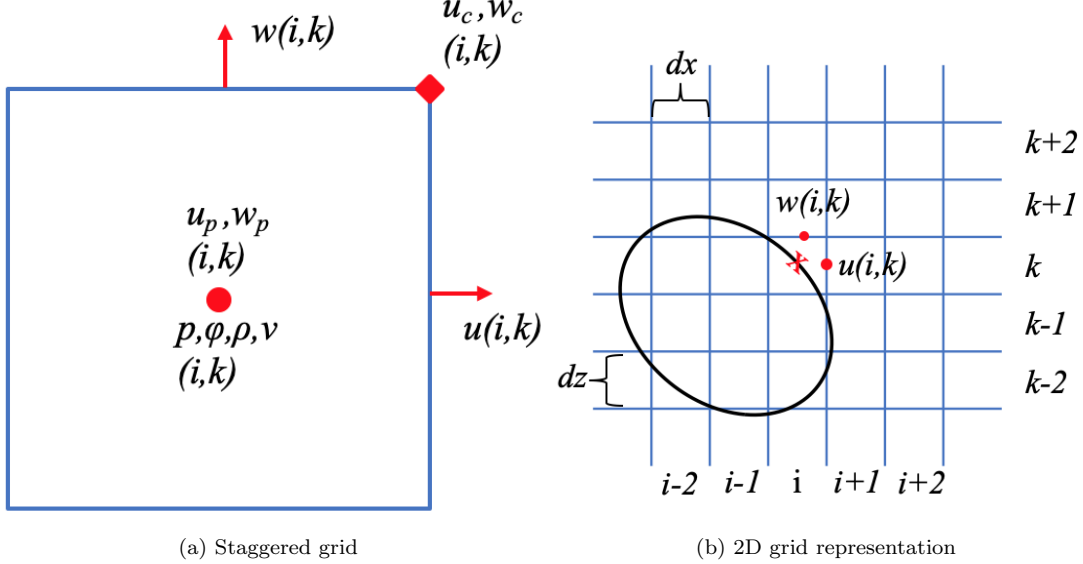
Fig. 1: (a) velocities and scalar quantities on a 3D staggered grid and (b) Representation of a 2D grid with current cell's velocities (red circles) and closest Lagrangian marker shown as 'x' located on the immersed boundary (solid black line).

2.1.3. Fractional-step method

Time advancement is achieved by the fractional-step method [38] via an explicit 3rd-order Runge-Kutta (RK) scheme formulated as follows:

$$\frac{\tilde{u}_i - u_i^{l-1}}{\Delta t} = \alpha_l \frac{\partial}{\partial x_j}\left(\nu \frac{\partial u_i^{l-1}}{\partial x_j}\right) - \alpha_l \frac{1}{\rho}\frac{\partial p^{l-1}}{\partial x_i} - \alpha_l\left(\frac{\partial u_i u_j}{\partial x_j}\right)^{l-1} - \beta_l\left(\frac{\partial u_i u_j}{\partial x_j}\right)^{l-2} + \alpha_l g_i \tag{13}$$

where a_l are the Runge-Kutta coefficients at each sub-step l and Δt the current time-step. In Hydro3D-NWT Δt is either set to a fixed value or is calculated during the simulation using the Courant–Friedrichs–Lewy criterion (CFL) and the viscous limit (VSL):

$$\Delta t_{CFL} = min\left(\frac{dx}{u_{max}}, \frac{dy}{v_{max}}, \frac{dz}{w_{max}}\right) \tag{14}$$

$$\Delta t_{VSL} = \frac{1}{|\frac{u_c}{dx}| + |\frac{v_c}{dy}| + |\frac{w_c}{dz}| + 2\nu\left(\frac{1}{dx^2} + \frac{1}{dy^2} + \frac{1}{dz^2}\right)} \tag{15}$$

and $\Delta t = min(\Delta t_{CFL}, \Delta t_{VSL}) \cdot sf$, where sf is a safety factor usually set to 0.2.

In the first Runge Kutta step ($l = 1$, $\alpha_1 = 1/3$), a non-divergence free velocity $\tilde{u}$ is obtained from the velocity and pressure filed calculated at the previous time-step (u_i^{t-1}, p^{t-1}) followed by an intermediate velocity for $l = 2$, $\alpha_2 = 1/2$. At the final RK step ($l = 3$, $\alpha_3 = 1$), the intermediate velocity $\tilde{u}_i$ is updated to $\tilde{u}_i^*$ by inclusion of the immersed boundary force f_i:

$$\tilde{u}_i^* = \tilde{u}_i + f_i \Delta t \tag{16}$$

2.1.4. Poisson equation

In Hydro3D-NWT, the updated velocity $\tilde{u}_i^*$ is coupled with a pseudo-pressure $\tilde{p}$ using the Poisson equation:

$$\frac{\partial}{\partial x_i} \left(\frac{1}{\rho} \frac{\partial \tilde{p}}{\partial x_i} \right) = \frac{1}{\alpha_l \Delta t} \frac{\partial \tilde{u}_i^*}{\partial x_i} \tag{17}$$

The Poisson equation is solved using an iterative multi-grid algorithm [39] in which all sub-domains are divided into smaller sized domains, at least twice, and the solution of the Poisson equation is obtained on the smaller sub-domain. Once the intermediate velocity $\tilde{u}_i^*$ satisfies continuity (Eq. (1)) the velocity and pressure of the current time step are updated in the corrector step as follows [38]:

$$u_i^t = \tilde{u}_i^* - \alpha_l \Delta t \frac{1}{\rho} \frac{\partial \tilde{p}}{\partial x_i} \tag{18}$$

$$p^t = p^{t-1} + \tilde{p} - \frac{\nu \alpha_l \Delta t}{2} \frac{\partial}{\partial x_j} \left(\frac{\partial \tilde{p}}{\partial x_j} \right) \tag{19}$$

2.2. Immersed boundary method

In Hydro3D-NWT solid structures are included in the flow domain using the diffuse direct forcing IB method described in [30]. In this method solid boundaries are represented via Lagrangian markers, at which an external force enforces the no-slip condition and these forces are added to the momentum equation, Eq. (2), in the respective fluid grid. One such Lagrangian marker is shown as 'x' in Fig. 1b. The non-divergence free velocity obtained from the 2nd RK step Eq. (13) is transferred to the closest Lagrangian marker from the nearest Eulerian fluid cell as:

$$U_{i_L} = \sum_{ijk=1}^{ne} \tilde{u}_{i_{ijk}} \delta(x_{i_{ijk}} - X_{i_L}) \Delta x_{i_{ijk}} \tag{20}$$

where U_{i_L} is the interpolated velocity at the Lagrangian marker using multiple neighbouring cells n_e and the discrete delta function δ defined as follows:

$$\delta(x_{i_{ijk}} - X_{i_L}) = \frac{1}{\Delta x_{i_{ijk}}} \phi \left(\frac{x_{ijk} - X_L}{dx} \right) \phi \left(\frac{y_{ijk} - Y_L}{dy} \right) \phi \left(\frac{z_{ijk} - Z_L}{dz} \right) \tag{21}$$

where $x_{i_{ijk}}$ and X_{i_L} are the locations of the Eulerian fluid cell and the nearest Lagrangian marker L, respectively. $\Delta x_{i_{ijk}} = dx \times dy \times dz$ is the volume of the fluid cell and ϕ the Kernel function from [40]. Then,

the required external force on the Lagrangian marker (F_{i_L}) needed to set a desired velocity (U_{i_*}) on the boundary of the structure is evaluated as:

$$F_{i_L} = \frac{U_{i_*} - U_{i_L}}{\Delta t} \tag{22}$$

and interpolated back to the fluid (Eulerian cell) as:

$$f_i = \sum_{ijk=1}^{ne} F_{i_L} \delta(x_{i_{ijk}} - X_{i_L}) \Delta V_L \tag{23}$$

where ΔV_L is volume of the current Lagrangian marker which is of the order of the cube of the Eulerian grid spacing. The current implementation has been validated using Hydro3D code in various engineering applications [41, 42].

2.3. Free-surface capturing

In Hydro3d-NWT, the level-set method (LSM) presented in [14] is employed to allow two-phase simulations and capture the evolution of the water surface. The implementation of the level-set method has been validated for open channel flows [43–45]. The LSM employs a signed distance function ϕ, at the cell's centre, as follows:

$$\phi(x,t) \begin{cases} < 0, & \text{if} \quad x \in \Omega_{gas} \\ = 0, & \text{if} \quad x \in \Gamma \\ > 0, & \text{if} \quad x \in \Omega_{liquid} \end{cases} \tag{24}$$

where cells with positive or negative ϕ values are occupied by air (Ω_{gas}) or liquid (or water) (Ω_{liquid}), respectively while the interface of the two (Γ) is defined by $\phi = 0$. ϕ is calculated from the pure advection equation:

$$\frac{\partial \phi}{\partial t} + u_i \frac{\partial \phi}{\partial x_i} = 0 \tag{25}$$

The spatial derivatives of ϕ are solved using a 5th-order weighted essentially non- oscillatory (WENO) scheme [16] which offers a good compromise between stability and accuracy of the solution. The main formulation of the WENO scheme is summarized below.

First, the velocity components (u_i) are interpolated at the centre of the cell using a four point stencil as follows:

$$\begin{aligned} u_{i-\frac{1}{2},j,k} &= \frac{1}{16}(-u(i-2,j,k) + 9u(i-1,j,k) + 9u(i,j,k) - u(i+1,j,k)) \\ v_{i,j-\frac{1}{2},k} &= \frac{1}{16}(-v(i,j-2,k) + 9v(i,j-1,k) + 9v(i,j,k) - v(i,j+1,k)) \\ w_{i,j,k-\frac{1}{2}} &= \frac{1}{16}(-w(i,j,k-2) + 9w(i,j,k-1) + 9w(i,j,k) - w(i,j,k+1)) \end{aligned} \tag{26}$$

8

A linear convex combination of three third order approximations $\dfrac{\partial \phi_{i+1/2}}{\partial x_i}^{(1)}$, $\dfrac{\partial \phi_{i+1/2}}{\partial x_i}^{(2)}$ and $\dfrac{\partial \phi_{i+1/2}}{\partial x_i}^{(3)}$ is used:

$$\frac{\partial \phi_{i+1/2}}{\partial x_i} = \omega_1 \frac{\partial \phi_{i+1/2}}{\partial x_i}^{(1)} + \omega_2 \frac{\partial \phi_{i+1/2}}{\partial x_i}^{(2)} + \omega_3 \frac{\partial \phi_{i+1/2}}{\partial x_i}^{(3)} \tag{27}$$

where $\dfrac{\partial \phi_{i+1/2}}{\partial x_i}^{(i)}$ is in the form of:

$$\frac{\partial \phi_{i+1/2}}{\partial x_i}^{(i)} = \gamma_1 \frac{\partial \phi_{i+\frac{1}{2}}}{\partial x_i} + \gamma_2 \frac{\partial \phi_{i+\frac{1}{2}}}{\partial x_i} + \gamma_3 \frac{\partial \phi_{i+\frac{1}{2}}}{\partial x_i} \tag{28}$$

where $i = 1, 2, 3$ and $\gamma_{1,2,3}^{(1)} = \dfrac{1}{3}, -\dfrac{7}{6}, \dfrac{11}{6}$, $\gamma_{1,2,3}^{(2)} = -\dfrac{1}{6}, \dfrac{5}{6}, \dfrac{1}{3}$ and $\gamma_{1,2,3}^{(3)} = \dfrac{1}{3}, \dfrac{5}{6}, -\dfrac{1}{6}$. The nonlinear weights $\omega_j = \omega_1, \omega_2, \omega_3$ are evaluated as:

$$\omega_j = \frac{\tilde{\omega}_j}{\tilde{\omega}_1 + \tilde{\omega}_2 + \tilde{\omega}_3} \quad , \quad \tilde{\omega}_j = \frac{\alpha_j}{(\varepsilon + \beta_j)^2} \tag{29}$$

where $\alpha_j = \alpha_{1,2,3} = 0.1, 0.6, 0.3$ and β_j defined as:

$$\beta_1 = \frac{13}{12} \left(\frac{\partial \phi_{i-2}}{\partial x_i} - 2\frac{\partial \phi_{i-1}}{\partial x_i} + \frac{\partial \phi_i}{\partial x_i} \right)^2 + \frac{1}{4} \left(\frac{\partial \phi_{i-2}}{\partial x_i} - 4\frac{\partial \phi_{i-1}}{\partial x_i} + 3\frac{\partial \phi_i}{\partial x_i} \right)^2$$

$$\beta_2 = \frac{13}{12} \left(\frac{\partial \phi_{i-1}}{\partial x_i} - 2\frac{\partial \phi_i}{\partial x_i} + \frac{\partial \phi_{i+1}}{\partial x_i} \right)^2 + \frac{1}{4} \left(\frac{\partial \phi_{i-1}}{\partial x_i} - \frac{\partial \phi_{i+1}}{\partial x_i} \right)^2 \tag{30}$$

$$\beta_3 = \frac{13}{12} \left(\frac{\partial \phi_i}{\partial x_i} - 2\frac{\partial \phi_{i+1}}{\partial x_i} + \frac{\partial \phi_{i+2}}{\partial x_i} \right)^2 + \frac{1}{4} \left(3\frac{\partial \phi_i}{\partial x_i} - 4\frac{\partial \phi_{i+1}}{\partial x_i} + \frac{\partial \phi_{i+2}}{\partial x_i} \right)^2$$

where ε is set to 1.0×10^{-6}. The first estimation of $\dfrac{\partial \phi_{i+1/2}}{\partial x_i}$ is obtained using a 2nd order CDS before applying Eqs. (27) to (30) and time advancement is achieved using a 3rd order Runge-Kutta scheme. The new free-surface location is then evaluated as:

$$\phi^t = \phi^{t-1} - \Delta t \left(u\frac{\partial \phi^{t-1}}{\partial x} + v\frac{\partial \phi^{t-1}}{\partial y} + w\frac{\partial \phi^{t-1}}{\partial z} \right) \tag{31}$$

where the superscript ^{t} denotes current time-step's properties whereas $^{t-1}$ are the values in an intermediate sub-step in the RK scheme.

To avoid discontinuities in fluid properties, especially near the interface, a Heaviside function $H(\phi)$ is employed to smoothly exchange properties between phases inside a transition zone of width 2ε where $\varepsilon = 2max(dx, dy, dz)$, as follows:

$$H(\phi) \begin{cases} = 0, & \text{if} \quad \phi < -\varepsilon \\ = \frac{1}{2}\left(1 + \frac{\phi}{\varepsilon} + \frac{1}{\pi}\sin\frac{\pi\phi}{\varepsilon}\right), & \text{if} \quad |\phi| \leq \varepsilon \\ = 1, & \text{if} \quad \phi > \varepsilon \end{cases} \tag{32}$$

and

$$\rho(\phi) = \rho_g + (\rho_l - \rho_g)H(\phi)$$
$$\mu(\phi) = \mu_g + (\mu_l - \mu_g)H(\phi)$$

(33)

where notations $_g$ and $_l$ represent gas and fluid variables. In the LSM the numerical domain is treated as a continuous fluid, hence velocities and pressure at the interface and inside the transition zone are calculated analogue to the rest of the domain and according to section 2.1. Finally, to secure that ϕ maintains its property the condition $|\nabla\phi| = 1$ is met using the re-initialization technique proposed by [46] applied inside the transition zone as:

$$\frac{\partial \phi}{\partial t_a} + s(\phi_0)(|\nabla\phi| - 1) = 0$$

(34)

where $s(\phi_0)$ is the smoothed signed function defined as:

$$s(\phi_0) = \frac{\phi_0}{\sqrt{\phi_0^2 + (|\nabla\phi_0|\varepsilon_r)^2}}$$

(35)

t_a is an artificial time calculated based on the grid size multiplied by a factor of less than one. $\phi_0(x,0) = \phi(x,t)$ and ε_r represents one grid size. In the following sub-section, a solitary wave propagating in a tank is simulated to validate the current implementation.

2.3.1. Run-up of a solitary wave

The propagation and run-up of a solitary wave in a tank is a classic benchmark case for testing two-phase flow models. The problem presented by Yue et al. [47] is considered to test the adequacy of the level-set method for the accurate prediction of the run-up of a solitary wave on a vertical wall.
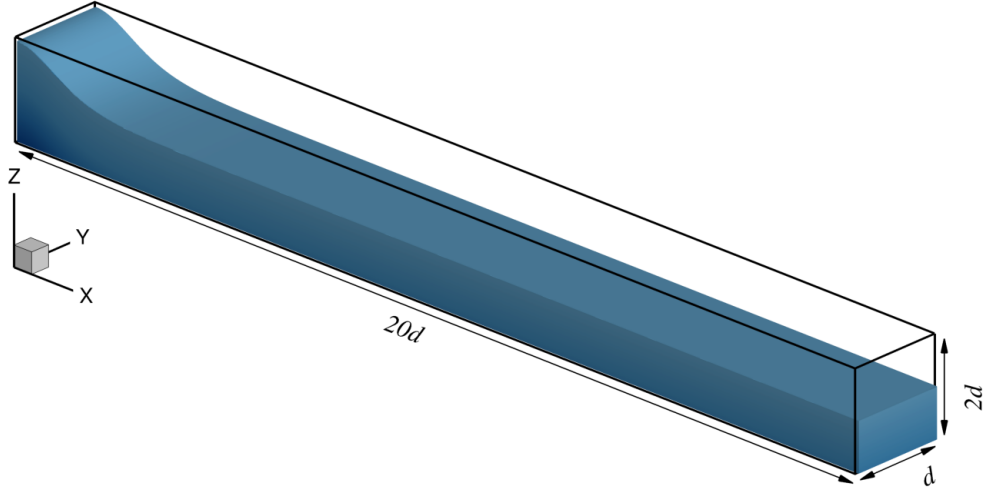
(a) 3D view
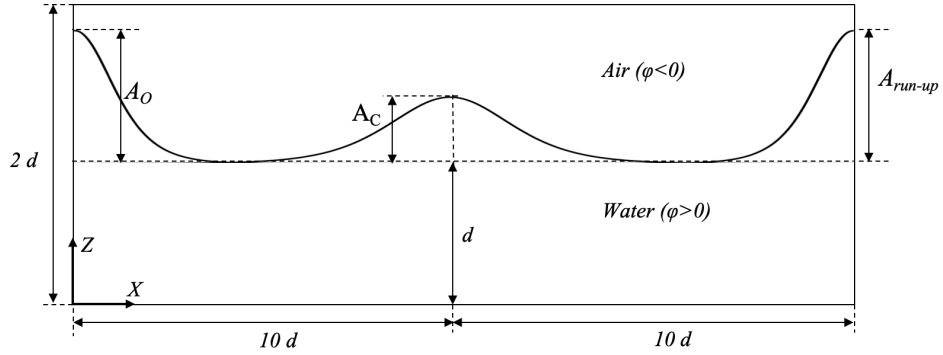
(b) Side view

Fig. 2: A schematic diagram of a three-dimensional solitary wave of height A_c propagating in a numerical tank from an initial height A_0 at $x = 0$, (a) 3D view and (b) side view.

Figure 2a shows a wave, initially at rest, the crest of which is A_0 above still water-level ($d = 1m$), before it is set free to propagate in a $20d \times d \times 2d$ ($x \times y \times z$) numerical tank, as sketched in Fig. 2b. The theoretical wave celerity is $C = \sqrt{gd} = 1.0 m/s$, the Reynolds number is $Re = Cd/\nu_2 = 5 \times 10^4$ and the viscosity and density ratios are set to $\nu_1/\nu_2 = 15$ and $\rho_1/\rho_2 = 1.2 \times 10^{-3}$ (subscripts $_1$ and $_2$ denote air and water properties, respectively). The domain is discretised with $640 \times 32 \times 128$ ($N_x \times N_y \times N_z$) uniform cells and a fixed time-step of $dt = 0.001$ sec is adopted. A no-slip boundary condition is applied at the west, east and bottom walls, while free to slip condition is employed at the top and side-walls. In the simulations, various initial wave heights are tested, $0.1 \leq A_0/d \leq 0.9$, all generated by initialising the free-surface based

11

on Boussinesq profile with zero initial velocity:

$$A(x,0) = A_0/cosh^2 \left(\frac{\sqrt{3A_0}}{2} x \right) \tag{36}$$
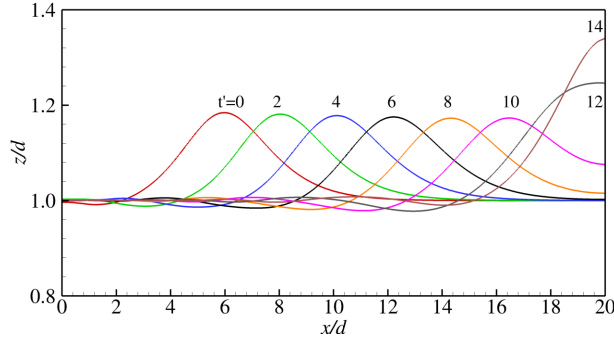
Fig. 3: Position of the solitary wave in the numerical tank at various time instances, $A_0/d = 0.4$

(a) Maximum run-up elevation.
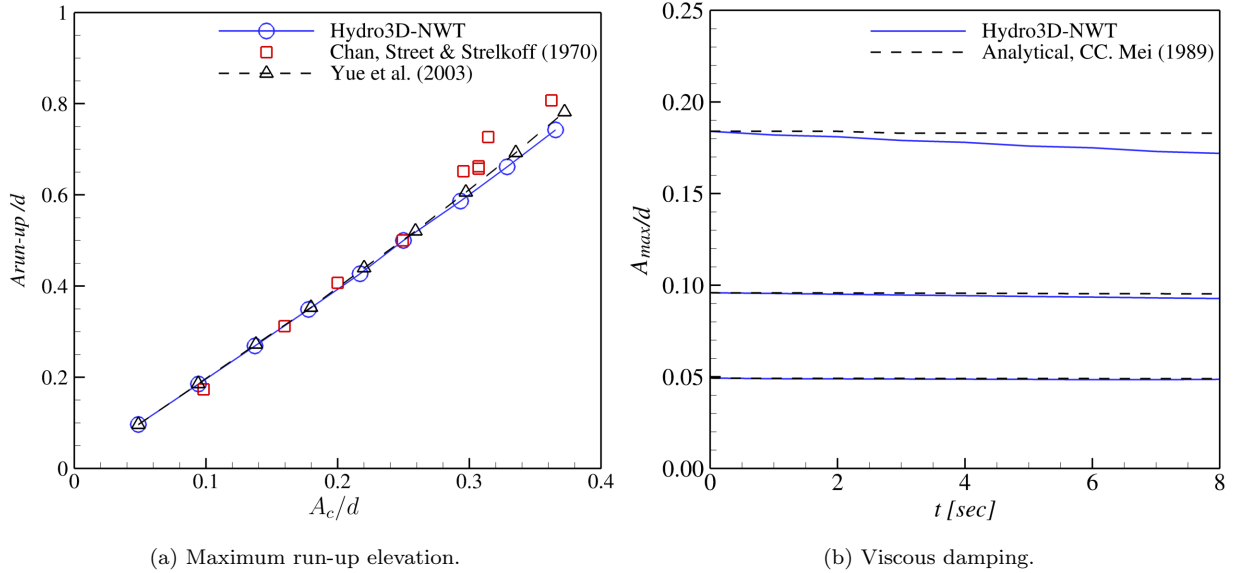
(b) Viscous damping.

Fig. 4: Comparisons between (a) simulations of the maximum run-up elevation (solid lines, open circles) with experimental data [48] (open squares) and other numerical results [47] (dashed lines, open deltas) and (b) Hydro3D-NWT's viscous damping (solid lines) and analytical solution [49] (dashed lines).

Figure 3 sketches the progression and run-up of the solitary wave with initial amplitude $A_0/d = 0.4$ in the numerical tank driven by gravitational and viscous forces. For visualization purposes, a time-measure t' is used and defined as $t' = 0$ when the west boundary (x/d=0) has no effect on the wave's motion and the wave behaves as a solitary wave. In the case of $A_0/d = 0.4$ this corresponds to $t = 6$ sec. Figure 4a plots the simulated run-up distance A_{run-up} (solid line, open circles) together with experimental data from Chan et al. [48] (open squares) and simulation data from Yue et al. [47] (dashed lines, open deltas). Various initial

12

conditions with different wave amplitudes are considered and the corresponding run-ups on the east wall (x/d=20) are obtained. The results compare well with the experiments and the other data of [47] , within 2% of error (ε) for smaller waves. However, minor deviations from the experimental data are observed with less than 10% error for large wave amplitudes ($A_c/d \geq 0.3$), similar to other numerical results [47]. Here, the error is defined as:

$$\varepsilon = \frac{|(Y_{exp} - Y_{num})|}{Y_{exp}} \times 100 \tag{37}$$

with Y set to A_{runup}/d. The computed viscous damping is plotted in Fig. 4b together with the analytical solution of [49]:

$$A_{max}^{-1/4} = A_{0max}^{-1/4} + 0.08356 \left(\frac{\nu_2 C^{3/2}}{d^{7/2}} \right)^{1/2} t \tag{38}$$

where A_{max} is the amplitude of the solitary wave and A_{0max} is the maximum initial amplitude. The viscous damping from Hydro3D-NWT agrees quite well with the analytical solution for $A_{max}/d \leq 0.1$ with an error of less than 1%, (based on Eq. (37), $Y = A_{max}/d$), while discrepancies are observed for larger waves, which are in part due to limitations of the analytical solution which is only valid for wave-heights of $A_0/d \leq 0.1$ [49] and probably in part due to the numerical scheme since WENO employed in LSM introducing some artificial dissipation, especially large water surface gradients. The results presented suggest that the LSM is able to provide accurate surface elevations and predicts well viscous damping.

2.4. Numerical wave tank

In order to produce accurate results from Hydro3D-NWT, it is important to compute consistent and accurate wave-elevations, according to the desired wave-theory, and effectively absorb incident waves to avoid interactions between incident and reflected waves.

2.4.1. Wave generation

In Hydro3D-NWT, waves are generated in the numerical flume using analytical solutions of the free-surface elevation and particles velocities, at the (inlet) west boundary (at $x = 0$). This is an efficient and quick method to generate most wave conditions of engineering interest. If uni-directional, 2nd-order Stokes waves are to be simulated in the NWT, the following equations are applied at the west boundary:

$$n = \frac{H}{2} \cos\left(\omega t - \frac{\pi}{2}\right) + \frac{H^2 k}{16} \left(3 \coth^3(kd) - \coth(kd)\right) \cos\left(2(\omega t - \frac{\pi}{2})\right) + d \tag{39}$$

$$u = \frac{H}{2}\omega \left(\frac{\cosh(kz)}{\sinh(kd)} \right) \cos\left(\omega t - \frac{\pi}{2}\right) + \frac{3}{16}\omega(kH)^2 \left(\frac{\cosh(2kz)}{\sinh^4(kd)} \right) \cos\left(2(\omega t - \frac{\pi}{2})\right) \tag{40}$$

$$w = -\frac{H}{2}\omega \left(\frac{\sinh(kz)}{\sinh(kd)} \right) \sin\left(\omega t - \frac{\pi}{2}\right) - \frac{3}{16}\omega(kH)^2 \left(\frac{\sinh(2kz)}{\sinh^4(kd)} \right) \sin\left(2(\omega t - \frac{\pi}{2})\right) \tag{41}$$

13

where H is the wave height and wave-number k related to wavelength L, is $k = \frac{2\pi}{L}$. Angular frequency ω is defined by the dispersion relation:

$$\omega^2 = gk\tanh(kd) \tag{42}$$

These equations are modified to account for the origin of the coordinate system (z=0 at floor bed) and that at $t = 0$ sec the water surface is at still water-level from which it moves upwards. The spanwise velocity, v, is set to zero to ensure that no secondary spanwise flow is generated at the inlet boundary. Pressure is not prescribed at the inlet boundary and is initialised as hydrostatic when the water surface is at still water level at $t = 0$ sec. The values of the signed distance function ϕ is prescribed at the west boundary at each time-step as follows:

$$\phi \begin{cases} = |z_c - n|, & \text{if} \quad z_c < n \\ = -|z_c - n| & \text{if} \quad z_c > n \\ = 0, & \text{if} \quad z_c = n \end{cases} \tag{43}$$

where z_c is the vertical coordinate of the centre of each cell and n the position of the water surface at each time step.

2.4.2. Wave damping

At the domain's outlet, waves are absorbed using the artificial damping method based on Choi and Yoon [50] or the relaxation method described in [20, 22], respectively. Herein, only the relaxation method is used for all simulations presented in the following. A detailed implementation of the artificial damping method can be found in [36, 50].

In the relaxation method, a relaxation function $\Gamma(X)$ is introduced to gradually reduce velocities and the signed distance function ϕ to zero, i.e. still water-level inside a zone near the outlet of the domain. Figure 5 shows different relaxation functions one may use, with $R = 3.5$ (solid line) or $R = 2$ (dashed-dot line) in Eq. (44) or a third degree polynomial (dashed line). In Hydro3D-NWT a relaxation function is employed as follows:

$$\Gamma(X) = 1 - \frac{e^{X^R} - 1}{e - 1} \quad , \qquad X = \frac{x - x_s}{x_e - x_s} = [0, 1] \tag{44}$$

where R is set to $R = 3.5$ and the length of the absorbing layer $(x_e - x_s)$ set to two wavelengths $(2L)$. Once the new location of the free-surface is obtained, Eq. (45) is applied inside the absorbing zone to retain still water-level. Velocities are updated based on Eq. (46) at every sub-step of the Range-Kutta scheme to achieve still water conditions. In the following equations, notation 'target' stands for the targeted value (i.e zero for the velocity components and still water-level for ϕ) and 'computed' is the simulated one.

$$\phi = (1 - \Gamma(X))\phi_{target} + \Gamma(X)\phi_{computed} \tag{45}$$

14

$$u_i = (1 - \Gamma(X))u_{i_{target}} + \Gamma(X)u_{i_{computed}} \tag{46}$$
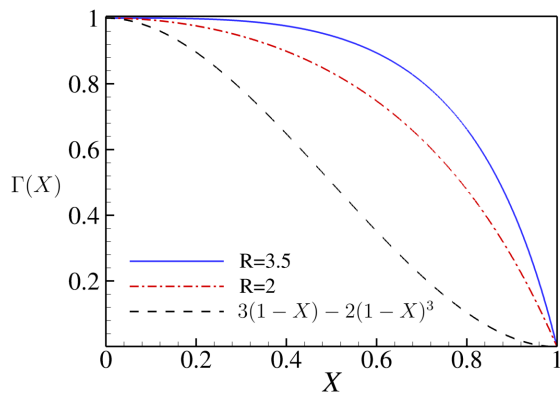
Fig. 5: Different relaxation functions. $R = 3.5$ (solid line) and $R = 2$ (dashed-dot line) in Eq. (44) or a third order polynomial (dashed line).

2.4.3. Periodic waves propagating in a numerical tank

In this section, simulations of nonlinear waves propagating along the computational domain are performed for various grid and time-step resolutions, with the goal to examine the reliability and accuracy of Hydro3D-NWT to generate, progress and absorb periodic waves. In the absence of a structure, wave theory can be used to validate Hydro3d-NWT's simulated wave-elevations and velocity profiles.

Figure 6 sketches a $38.4d$ long, $0.8d$ wide and $2d$ tall 3D numerical wave tank inside which nonlinear Stokes waves are generated at the west boundary and are absorbed near the opposite end (east boundary) inside a two wavelength-long ($2L$) relaxation zone. Analytical solutions are used to prescribe the water surface and velocities at the west boundary based on 2nd-order Stokes theory for a wave height of $H/d = 0.15$ and a wavelength of $L/d = 4$ in a $d = 0.5m$-deep NWT. Based on Eq. (42) the corresponding wave period is $T = 1.18$ sec. The current wave parameters are chosen to simulate realistic, relatively steep waves propagating in intermediate water depths. Dirichlet and Neumann boundary conditions for velocities and the signed distance function ϕ are applied at the west and east boundaries, respectively while sidewalls and the top boundary are set to free slip walls. At the bottom a no-slip wall boundary condition is used to resolve the boundary layer and near-wall viscous damping. Waves are generated in the NWT for $70T$ to examine the performance of the model over a long simulation time. Table 1 lists the various grid resolutions for a grid convergence study with $dx/d = (0.05, 0.025, 0.0125)$ and $dz/d = (0.025, 0.0125)$. In all cases, the spanwise and streamwise grid spacings are equal ($dy = dx$). Finally, four different time step sizes are adopted to examine the effect of time discretisation featuring maximum Courant–Friedrichs–Lewy numbers of $CFL = (0.4, 0.2, 0.1, 0.05)$, respectively.
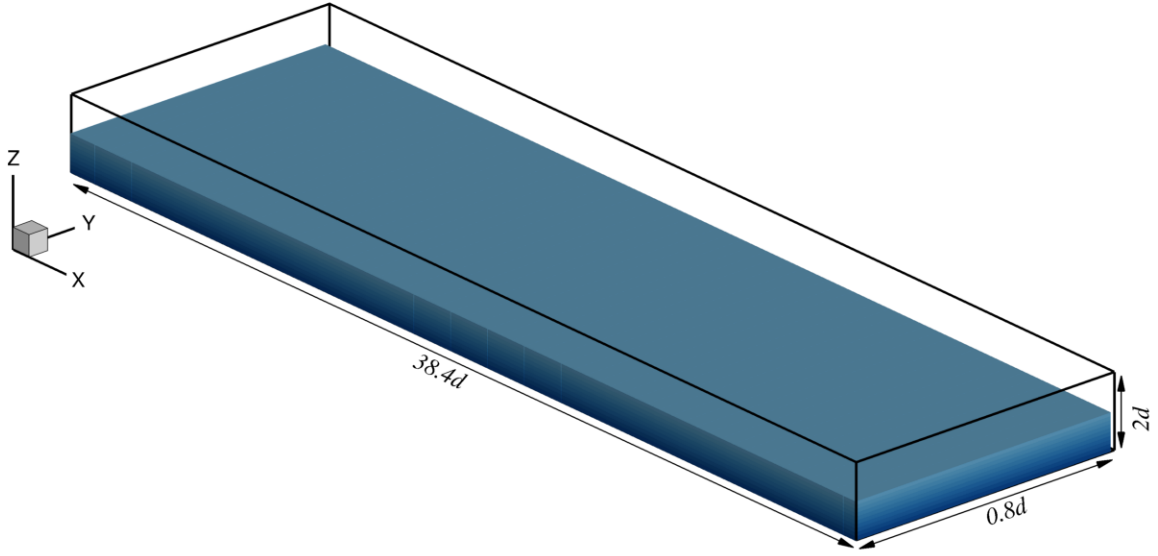
(a) 3D view
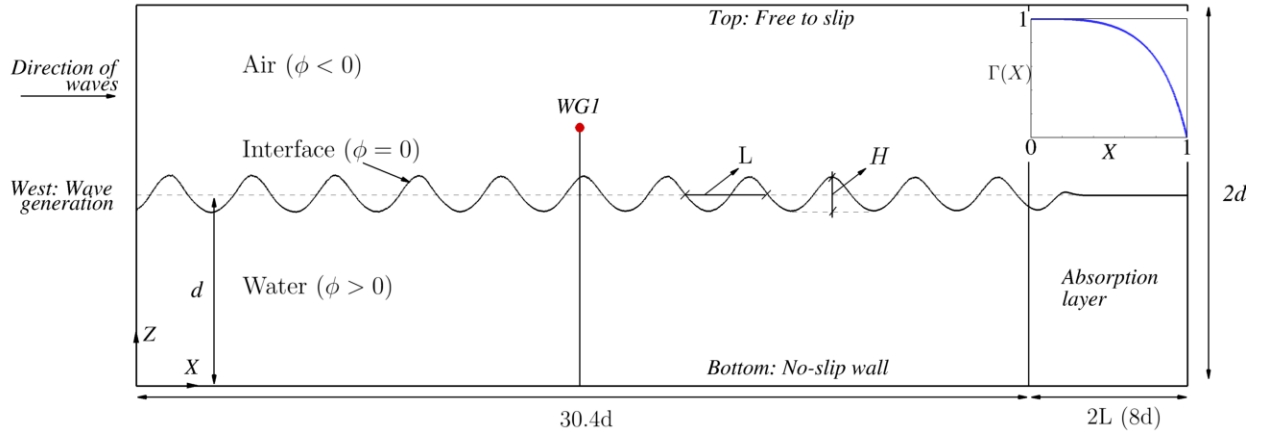
(b) Side view

Fig. 6: A schematic diagram of 2nd order Stokes waves propagating in the NWT along with the representation of the absorbing layer (top-right block) and wave-gauge's location.

Table 1: Spatial resolution parameters of the non-dimensional grid size followed by the number of cells in each direction (N_i)

	dx/d	dy/d	dz/d	N_x	N_y	N_z
Case 1	0.05	0.05	0.025	768	16	80
Case 2	0.025	0.025	0.025	1536	32	80
Case 3	0.025	0.025	0.0125	1536	32	160
Case 4	0.0125	0.0125	0.0125	3072	64	160

16
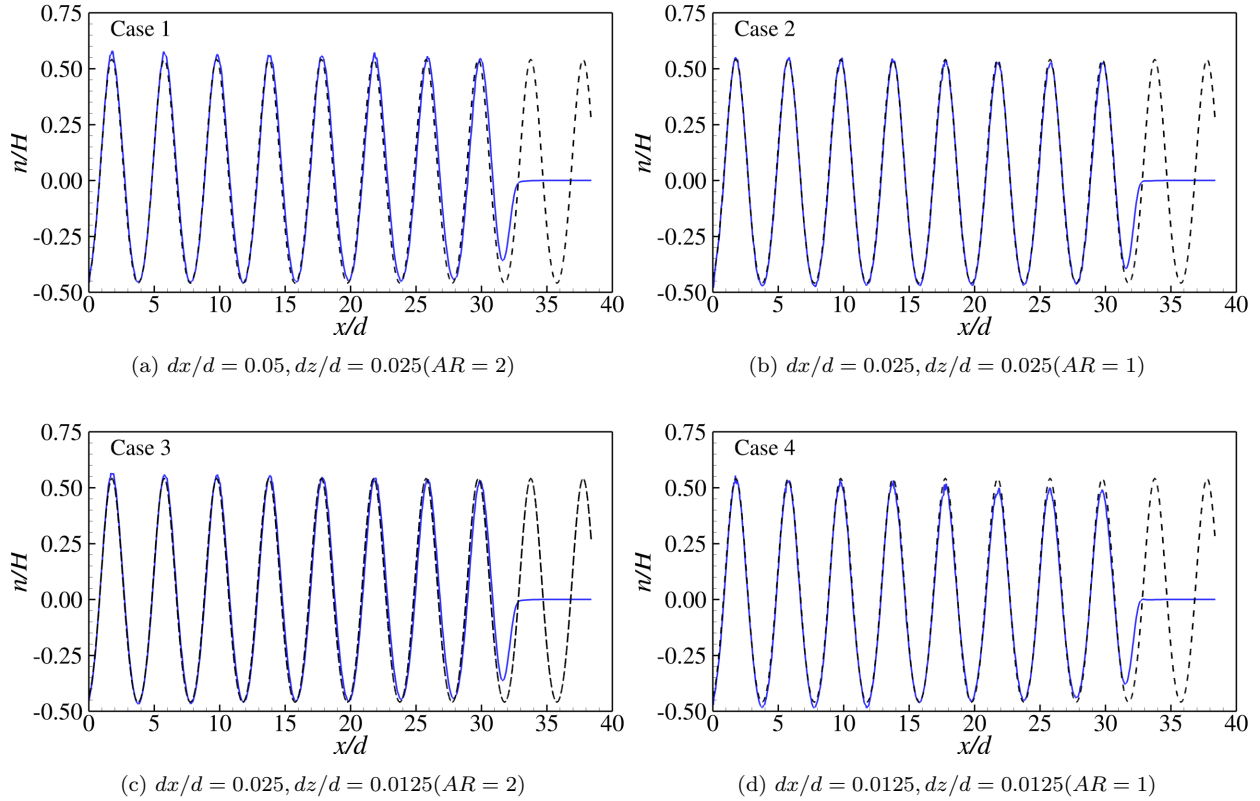
Fig. 7: Comparisons of the free-surface elevation after $70T$ for different grid resolutions with a fixed time-step of $dt = 0.001$ sec between Hydro3D-NWT (solid blue lines) and analytical solution (dashed black lines).

Figure 7 plots calculated non-dimensional wave elevations n/H (solid lines) as a function of distance from the upstream boundary together with 2nd order Stokes theory (dashed lines), at the center-line of the domain, for various grid resolutions and for a fixed time-step of $dt = 0.001$ sec. Wave elevation n measures the distance of the water surface from still water level with $n = 0$ at $z = d$ ($z = 0$ at the bottom of the tank). The accuracy and convergence of the simulations are examined in terms of the error between computed and analytically obtained vertical locations of wave crests ϵ_c and troughs ϵ_τ as well as the dispersion error ϵ_d. The dispersion error is measured as the error between the computed and analytical solutions as obtained at the crests and troughs in the tank. These are calculated at the final time-step and averaged in the streamwise direction and are provided in Table 2. Hydro3D-NWT predicts well the wave elevation with a maximum error of 0.36% in the vertical location of crests and troughs and a maximum dispersion error of 0.51% for the coarsest grid in Fig. 7a, whereas results improve with finer grid resolutions. In Fig. 7b and Fig. 7c the simulations accurately predict the troughs and crests locations along the full domain and results compare well with the corresponding wave theory. In Case 3 ($dx/d = 0.025$ and $dz/d = 0.0125$) the wave amplitude is improved, though a slightly higher dispersion error is observed in comparison with case 2 ($dx/d = 0.025$ and $dz/d = 0.025$). Minor underestimation of the crests in the finest case, Fig. 7d is observed towards the end of

the domain, due to higher dissipation inside the transition area between the two phases. Due to limitations in the level-set method and the relatively steep waves, the number of cells across the transition zone has to be chosen such to ensure the stability of the free-surface capturing model which appears to be to the detriment of its accuracy. For the finest grid, this is 4 cells on either side of the interface (compared to 2 cells for all other simulations) and this increases the damping near the interface. In terms of dispersion error, all simulations produce accurate results in terms of wavelength matching the theoretical value throughout the numerical domain with the coarsest resolution slightly overestimating the wavelength towards the end of the domain. Overall, wave elevations compare well with 2nd order Stokes theory while vertical grid refinement improves the elevations of crests and troughs (ϵ_c and ϵ_τ) and the dispersion error is reduced with finer horizontal grid resolution.

Table 2: Stream-wise average errors of the vertical location of crest and troughs, ϵ_c and ϵ_τ and average dispersion error ϵ_d.

	dx/d	dy/d	dz/d	ϵ_c	ϵ_τ	ϵ_d
Case 1	0.05	0.05	0.025	0.36%	0.11%	0.51%
Case 2	0.025	0.025	0.025	0.007%	-0.18%	0.045%
Case 3	0.025	0.025	0.0125	0.15%	0.04%	0.42%
Case 4	0.0125	0.0125	0.0125	-0.23%	-0.11%	-0.05%

Figure 8 presents a convergence study investigating the effect of temporal resolution using the spatial resolution of case 3, shown in Table 1. Four additional simulations are performed with different CFL criteria and the results of the simulations (solid lines) are compared with 2nd order Stokes theory (dashed lines). The coarsest time-step is based on CFL=0.4 in Fig. 8a which results in relatively large underpredictions of crests and troughs vertical locations, whereas the wavelength is mostly underestimated. Both errors in wave amplitude and wavelength are more significant near the relaxation zone. For finer time steps, the wavelength is well predicted however minor underestimation of the crests is observed near the end of the domain in Fig. 8b. Beyond that, crests and troughs are accurately predicted by Hydro3D-NWT and results improve with finer temporal discretisation and wave elevation presented in Figs. 8c and 8d match well with the theoretical solution.

Overall, the results suggest that grid and temporal convergence is achieved for $dx/d = dy/d = 0.025$, $dz/d = 0.0125$ and for $CFL = 0.1$ and finer simulations do not improve the predictions of Hydro3D-NWT for this particular problem. Consequently, a grid resolution similar to case 3 and a variable time step based on $CFL_{max} = 0.1$ is adopted to further verify Hydro3d-NWT for flow velocities and mass conservation properties. The latter is important in multi-phase simulations in particular when water levels vary significantly, as is the case in waves.

Figure 9 plots the relative volume V_{tot}/V_{init} as a function of time in the numerical wave tank, where V_{tot} is the total volume of water at each time step and V_{init} is the initial volume of water at $t = 0$ sec. An initial

18
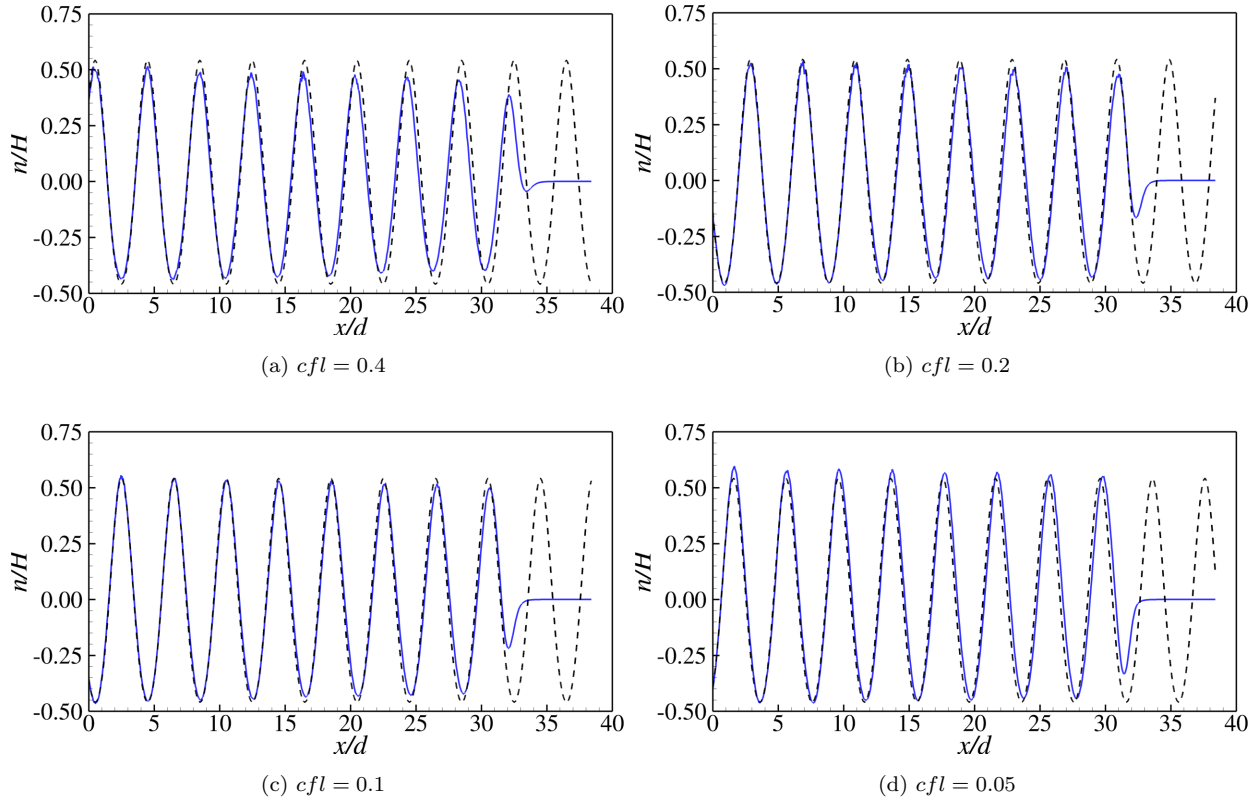
Fig. 8: Comparisons of the free-surface elevation after $70T$ for different temporal resolutions between Hydro3D-NWT (solid blue lines) and analytical solution (dashed black lines).

increase in the water volume is observed until about 10 sec at which the fist wave reaches the opposite end of the tank. Beyond that point, the volume drops and remains at a constant level above the initial value for the rest of the simulation.

Figure 10a plots the wave elevation during the last wave-period at WG1, i.e. at the centre of the effective domain ($x/d = 15.2$) and Figs. 10b and 10c plots simulated horizontal and vertical velocity profiles (solid lines) together with theoretical values (dashed lines, open squares) for various time steps at WG1. The velocities shown here represent the spanwise average of the horizontal and vertical velocity components plotted as a function of normalized vertical distance $z/(d + n)$ every $T/4$ starting at $t'/T = 0.25$ where $t' = t_{final} - T$ and t_{final} is the final simulated time. Both velocity components are well captured by Hydro3D-NWT and the results match well with the profiles obtained from 2nd order Stokes theory. In all cases, the error between numerical and theoretical velocity profiles is within 2%, while minor deviations, of less than 5% between simulated and theoretical horizontal velocity profiles are observed near the tank bottom. This is expected, since the theoretical solution is based on inviscid and irrotational flow whereas the simulations account for viscous effects with the bottom of the tank being treated as a no-slip wall. This results in a boundary layer near the wall which is visible from the horizontal velocity profiles. This wall has

19
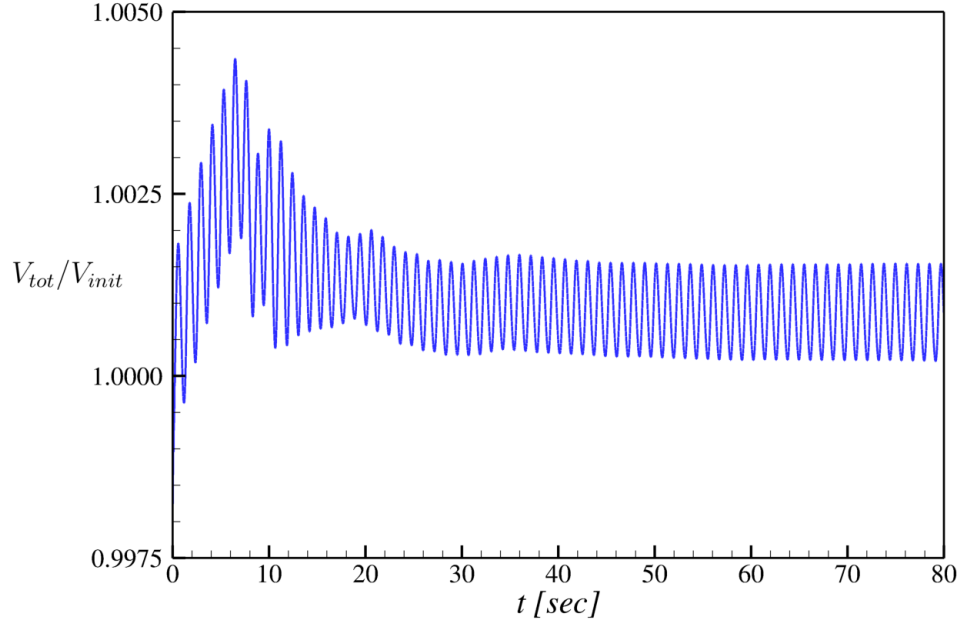
Fig. 9: Calculated relative volume of water over time in the numerical wave tank for $dx/d = 0.025$, $dz/d = 0.0125$, $cfl = 0.1$

no effect on the wall-normal velocity, hence both simulated and theoretical profiles agree well throughout the depth. The interaction of the two phases and the non-sharp transition of fluid properties at the air-water interface, create some small disturbances in the velocity field near the water surface, mostly observed in the horizontal component at $t/T = 0.25$, which could be reduced by local mesh refinement around the interface.

In general, Hydro3D-NWT is able to generate, progress and absorb non-linear waves in a tank. The grid resolution and time step convergence study suggests that Hydro3D-NWT predicts accurately water-level elevations along the tank and calculations of the water velocities below the water surface agree very well with the theoretical solutions.

20
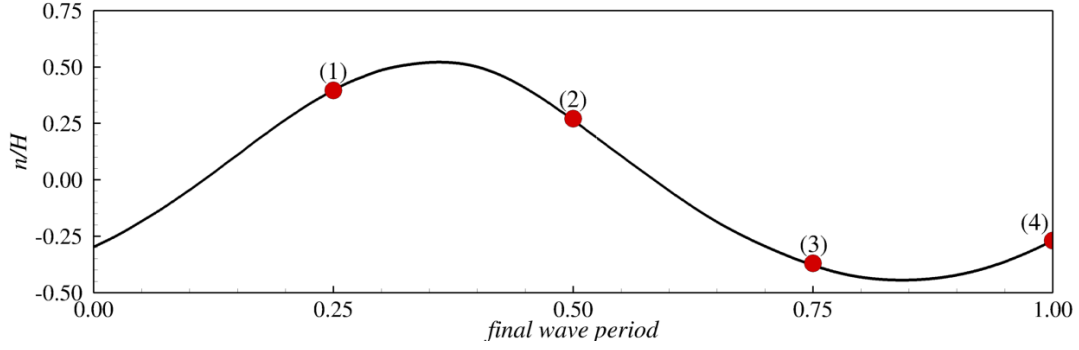
(a) Wave elevation
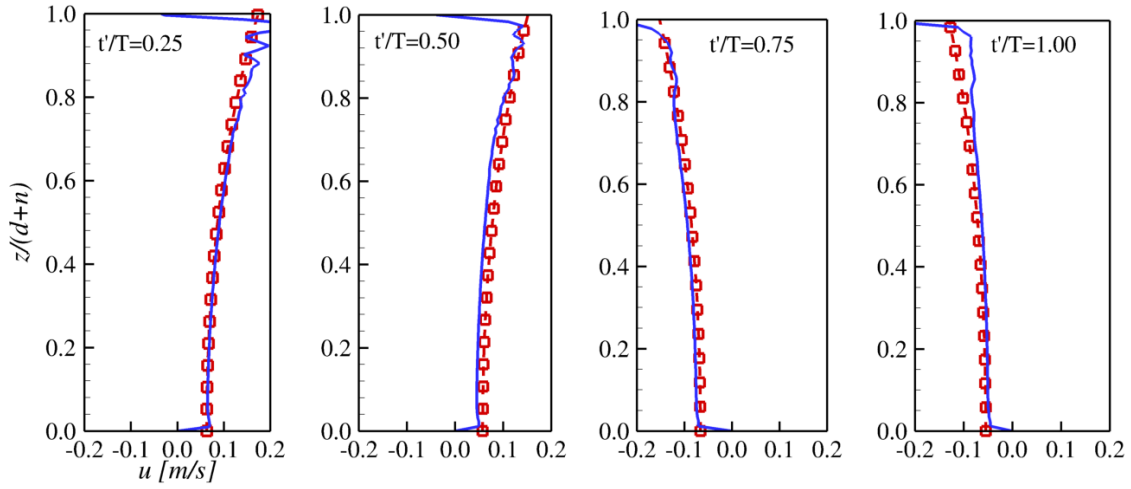
(b) Horizontal particles velocity
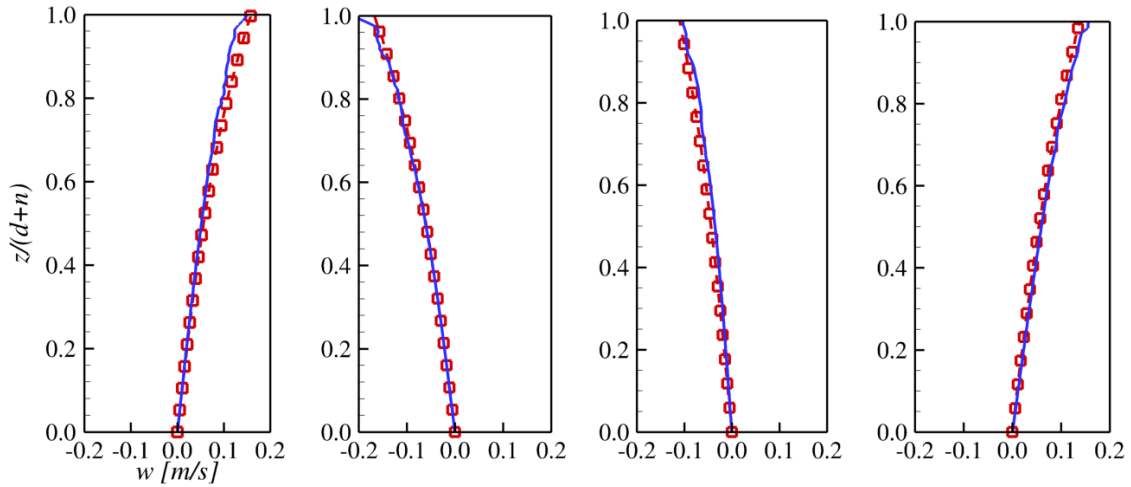
(c) Vertical particles velocity

Fig. 10: Comparisons of the horizontal and vertical velocity profiles between Hydro3D-NWT (solid blue lines) and 2nd order Stokes theory (dashed red line, open squares) at various time-steps over a wave-period at WG1 location. The top panel represents the final wave elevation at the same location as recorded by WG1 and the interval between markers 1-4 is $0.25T$.

3. 3D wave-structure interaction

Large-eddy simulations of non-linear waves interacting with complex solid structures are conducted to examine the performance and accuracy of Hydro3D-NWT when applied to realistic WSI problems. Stokes or cnoidal waves interacting with submerged obstacles as well as a solitary wave propagating over a flat plate, for which data of previous laboratory experiments are available, are considered. Hydrodynamic properties such as dynamic forces and pressures, water velocities and water levels are presented and compared with the data.

3.1. Monochromatic waves over a submerged trapezoidal bar
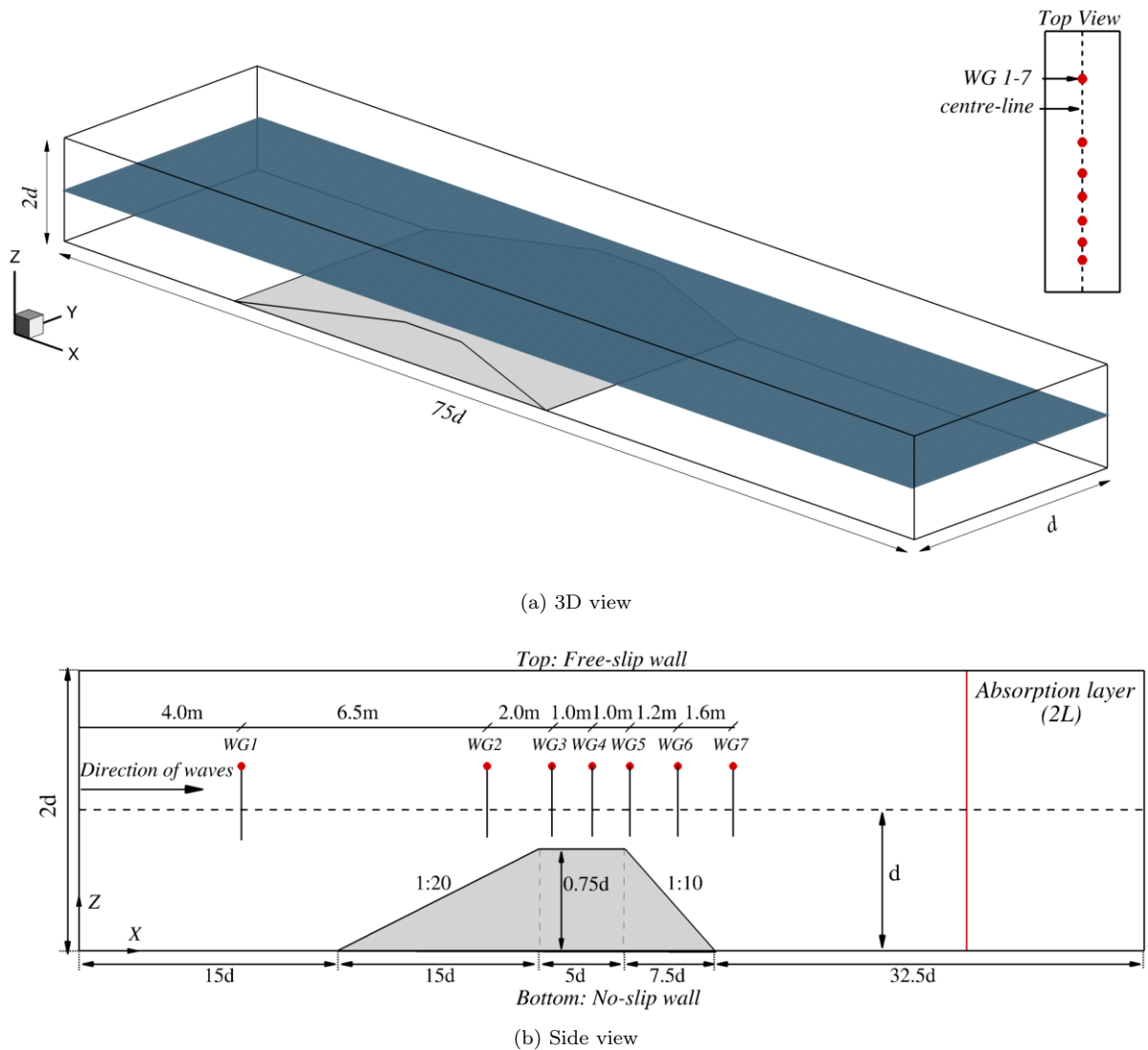
(a) 3D view

(b) Side view

Fig. 11: Schematic diagram of monochromatic waves traveling over a trapezoidal bar (a) in a 3D view and (b) from a side-view among with wave-gauges locations.

22

Waves interacting with submerged structures are challenging benchmark cases for NWTs. First of all, monochromatic waves propagating over a submerged trapezoidal bar, is simulated by Hydro3D-NWT. This WSI problem was studied via a laboratory experiment [51], data of which is being used to validate the simulation's accuracy.

Figure 11 sketches the submerged trapezoidal bar inside a $75d \times d \times 2d$ ($L_x \times L_y \times L_z$) and $d = 0.4m$ deep, NWT. The bar is located $15d$ from the wave-maker and anchored to the bottom and side-walls of the tank. The structure's height extends to $0.25d$ below still water-level and a $1:20$ and $1:10$ upstream and downstream slopes form the trapezoidal geometry of the bar. Seven wave-gauges along the centre-line of the flume, record the wave elevation in the tank. Incident waves of wave-height $H/d = 0.05$, wavelength $L/d = 9.325$ and wave-period $T = 2.0$ sec are generated using 2nd order Stokes theory at the west boundary. A uniform grid resolution of $dx/d = 0.025$, $dy/d = 0.025$ and $dz/d = 0.0125$ is used to discretise the numerical domain whereas a variable time-step, based on a maximum CFL number of $CFL = 0.1$ is adopted. Dirichlet and Neumann conditions for velocities and water surface surface are applied to the west and east boundaries, respectively. Sidewalls and the top boundary are treated as free-slip walls whereas a no-slip wall condition is employed at the bottom of the tank. Waves are absorbed near the east boundary, over a two wavelength ($2L$) relaxation zone to avoid reflections and simulations are run for eight wave-periods (8T) with the first three transient waves being ignored from the following calculations. For this reason, in the following figures, the time $t[sec]$ matches the ones in [52]. For example, t=0 sec is the instant at which the particular wave probe starts recording data.

Figure 12 presents the calculated wave profiles (solid lines) together with experimental data (open squares) demonstrating that Hydro3d-NWT reproduces accurately the waves of this particular case.
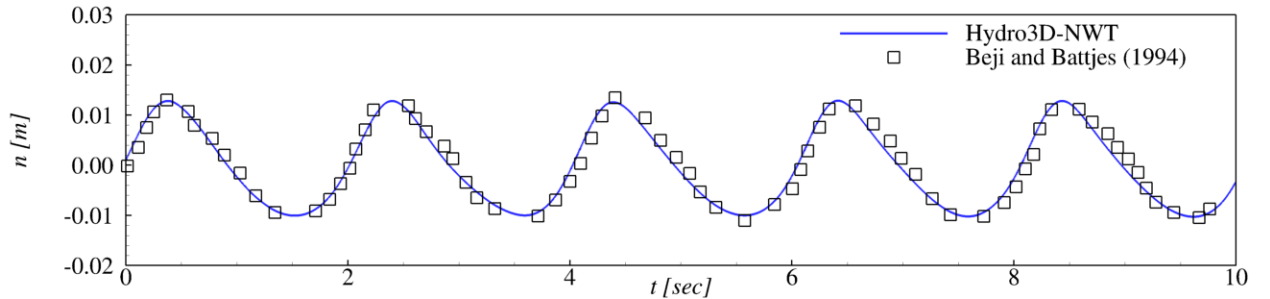
Fig. 12: Simulated (solid lines) and measured [52] (open squares) incident waves as recorded by WG1.

In Fig. 13, simulated wave elevations (solid lines), phase-averaged using the last five wave-periods, are plotted together with the experimental data (filled circles).Phase-averaged wave-elevations $\bar{n}$ can be calculated from the instantaneous elevations at the same phase as:

$$\bar{n}(t) = \frac{1}{N} \sum_{j=1}^{N} n(t + jT) \tag{47}$$

where $n(t + jT)$ is the wave-elevation at the j-th wave-period and N is the total number of wave-periods; in

23
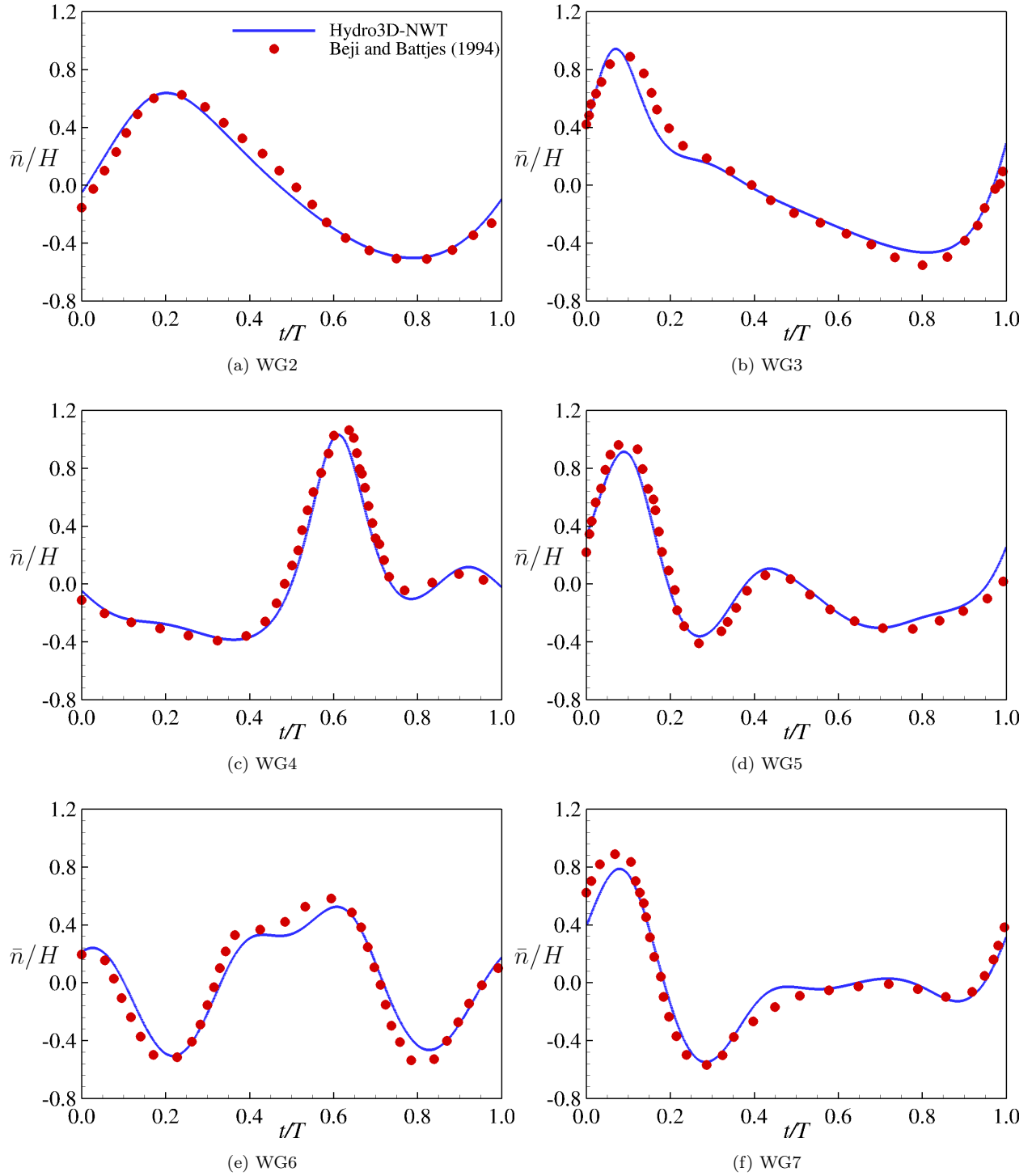
Fig. 13: Comparisons of the simulated phase averaged wave elevations (solid lines) with laboratory experiments [52] (filled circles) as recorded by (a)WG2-(f)WG7.

^{375} this case $N = 5$. At all wave gauge locations, Hydro3D-NWT produces accurate wave elevations matching very well those recorded in the laboratory experiment. A maximum average error, $\bar{\epsilon}$, of less than 1% is achieved with a maximum instantaneous error, ϵ, of less than 2% near the waves' crests. ϵ is calculated using the numerical results and the experimental data [51], shown in Fig. 13, based on the following:

$$\epsilon = \left| \frac{n(t) - n_{exp}(t)}{n_{exp}(t)} \right| \times 100 \tag{48}$$

where $n(t) = \bar{n}(t)/H + d$. Then a time-average, over one wave-period is employed, to evaluate the average ^{380} error $\bar{\epsilon}$ for each wave gauge. At WG2 (Fig. 13a), steeper waves and elongated asymmetrical troughs are formed owing to non-linear effects due to the sudden change in water depth as waves propagate over the upstream slope (1 : 20). The wave crests and troughs are well captured by Hydro3D-NWT. The waves continue to grow while propagating further downstream and over the top-flat surface of the structure, at WG3 (Fig. 13b) and WG4 (Fig. 13c). The progression of the waves is well simulated at these locations ^{385} however, at WG3, the simulated crest occurs a fraction earlier than in the experiment and the following trough is slightly underestimated. Wave-gauges WG5-WG7 (Figs. 13d to 13f), record a drop in wave-height due to energy dissipation and higher harmonic secondary waves are observed, following the experimental measurements, as a non-linear effect of the interaction of the waves with the submerged bar. Overall, the water-level fluctuations and progression of the waves over the are well captured by Hydro3D-NWT and ^{390} results suggest that the level-set method coupled with the current immersed boundary method can efficiently describe such WSI problems.

(a) Top view
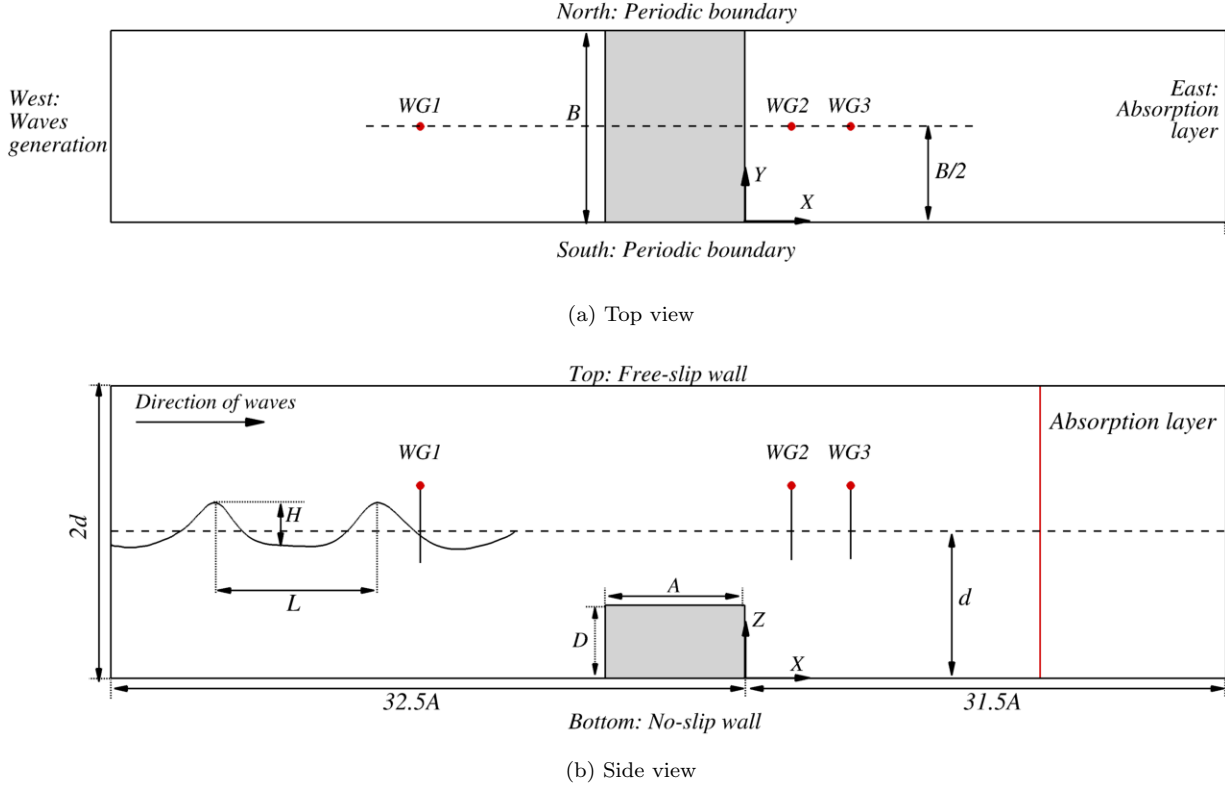
(b) Side view

Fig. 14: (a) A top view and (b) side view of cnoidal waves propagating in a 3D NWT over a submerged step.

Simulations of cnoidal waves propagating over a submerged step are performed in an attempt to reproduce accurately the laboratory experiment conducted by [53]. This WSI problem features dominant periodic flow separation at the step's leading and trailing edges and subsequent roll-up of large eddies. Figure 14 sketches a $d = 0.24m$ deep water-tank inside which cnoidal waves propagate over a submerged step of length $A = 0.4m$ and height $D/d = 0.5$. The step spans the full width of the tank and is located $32.5A$ away from the wave-maker. The NWT measures $64A \times B \times 2d$ $(L_x \times L_y \times L_z)$ where $B = 0.6m$ is the width of the step. In [53], three wave-heights were tested, however simulations are carried out for the case with wave-height $H/d = 0.15$, wavelength $L/d = 12.375$ and wave-period $T = 2.0$ sec. These conditions correspond to a relatively high Reynolds number of $Re = \dfrac{u_m d}{\nu} = 1.18 \times 10^5$, that is based on maximum particle velocity u_m, water-depth d and viscosity ν. Waves are generated at the west boundary based on analytical solutions of the free-surface elevation and particle velocities as proposed by [54].

A relatively fine uniform grid resolution of $dx/d = dy/d = 0.0125$ and $dz/d = 0.00625$ is adopted to make sure that flow separation and subsequent vortex shedding are captured properly. A variable time step, based on a maximum CFL number of $CFL = 0.1$ is applied and similar boundary conditions to the simulation of

Section 3.1 are adopted. A simulation time of 18 sec is computed whereas the first three wave-periods are ignored to make sure that waves and turbulence are fully developed. Three wave-gauges, WG1-WG3 are placed inside the flume to capture wave elevations, both upstream and downstream of the submerged step, and plots of the local velocity vector field and velocity profiles near the step's leading and trailing edges are presented.

Figure 15 plots the simulated wave elevations of the last six waves as recorded at WG1-WG3 (solid lines) together with the experimental data (open squares) in terms of the time series t', to account for the different wave generation methods adopted in experiments and simulations. t' is defined as $t' = 0$ when the first wave crest reaches the particular wave gauge. Good agreement is achieved at all locations. At WG1, the water elevations remain almost unchanged compared to the incident wave whereas at WG2 and WG3, both located downstream of the submerged obstacle, wave steepening and higher crests are observed, as well as weak secondary harmonics at WG3 as a result of the wave-structure interaction. At WG2, the simulated waves agree with those measured in the laboratory and similar to WG1, the water level in the troughs is slightly underestimated. This might be due to the cnoidal wave-theory adopted here to generate waves at the upstream end of the tank and might be improved with the adoption of higher order theories. The calculated water elevations at WG3, are in a good agreement with the experiments and the waves' shape is well captured. In the following figures, plots of the local velocity field, at various locations and instants, are presented to quantify the flow structure near the step and highlight the unsteady formation of local eddies due to flow separation.

Figure 16 plots the water level of the fifth wave that propagates over the trailing edge, as if it was recorded by a wave gauge. This follows the approach of [53] whereby the wave as recorded at WG2 is transferred to the trailing edge's location ($x = 0m$), using the wave celerity and assuming that waves remain unchanged over a short distance. This could be done by adding an additional wave gauge in the NWT but the above method was adopted in order to be consistent with the laboratory study. Two instants in time are considered, marked as (1) and (2) in Fig. 16 at which the velocity field near the step's trailing edge is visualised.

27
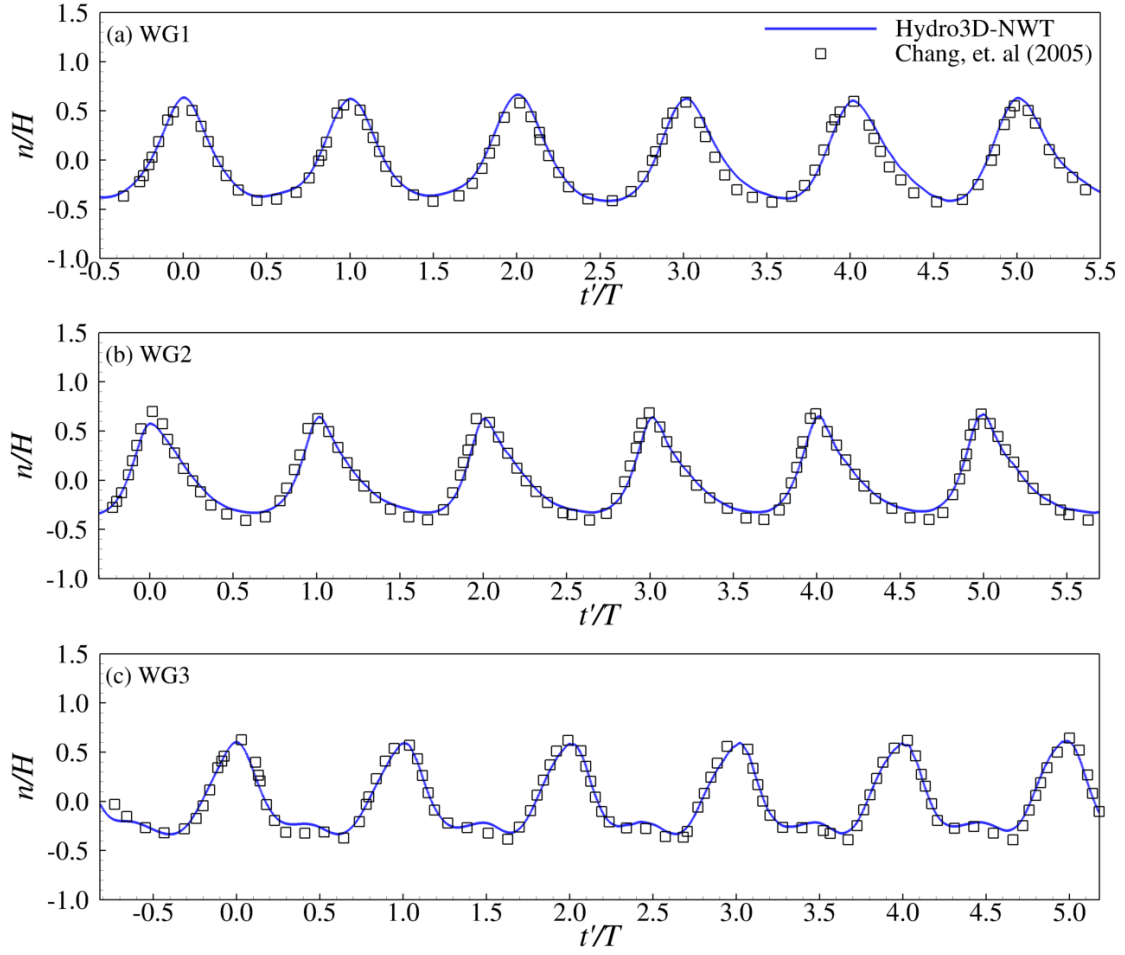
Fig. 15: Simulated wave elevations (solid lines) and experimental data [53] (open squares) at (a) WG1, (b)WG2 and (c)WG3.
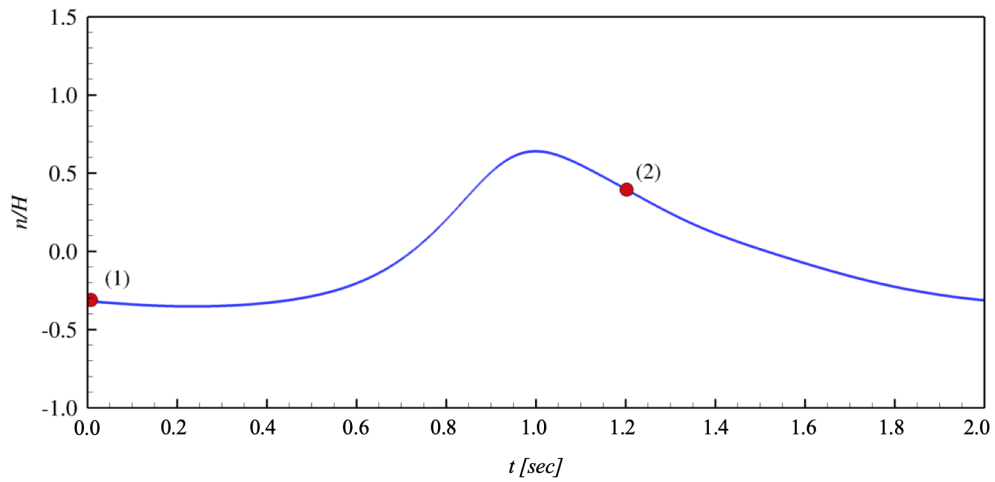

Fig. 16: Wave above the trailing edge of the step. Markers (1) and (2) represents instants in time at which velocity vectors and local velocity profiles are plotted in Fig. 17 and Fig. 18, respectively.
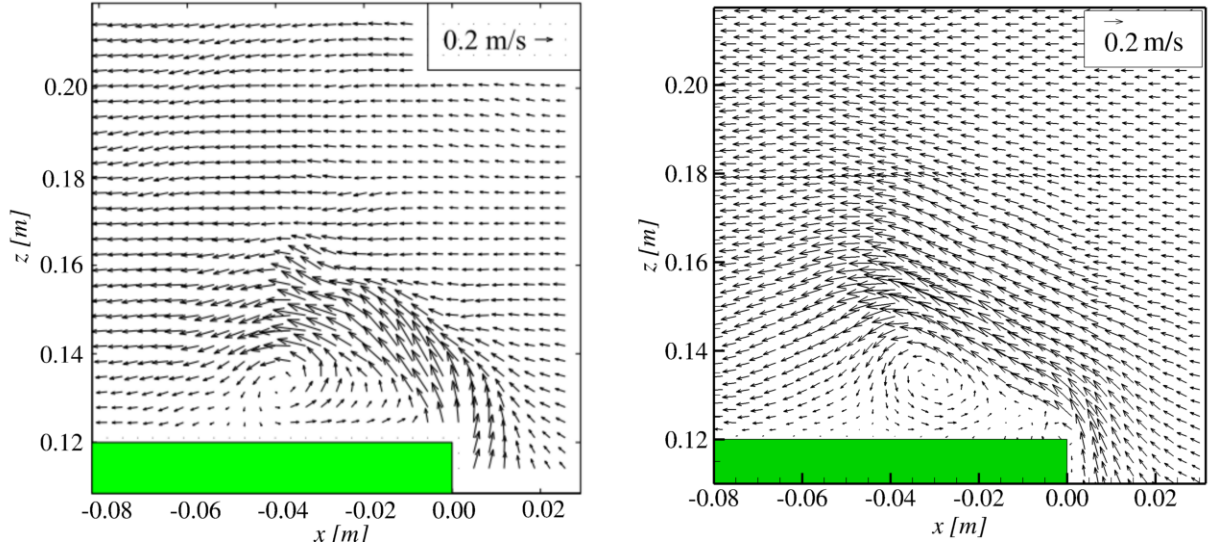
(a) Velocity vectors
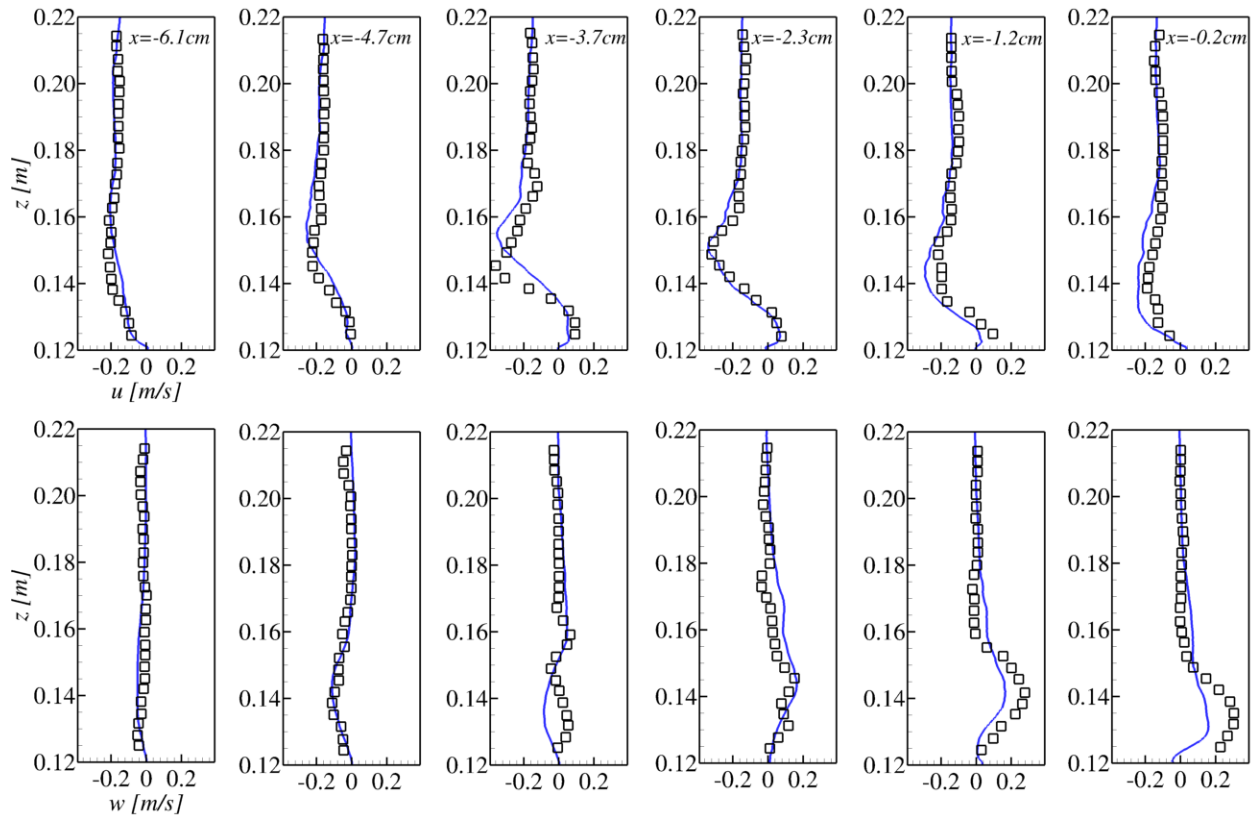
(b) Velocity profiles of the horizontal and vertical velocity

Fig. 17: (a) Simulated (right) and PIV-measured (left) instantaneous velocity vectors and (b) LES-predicted (solid lines) and measured (open squares) profiles of the the horizontal (upper row) and vertical (lower row) velocities at t=0s.
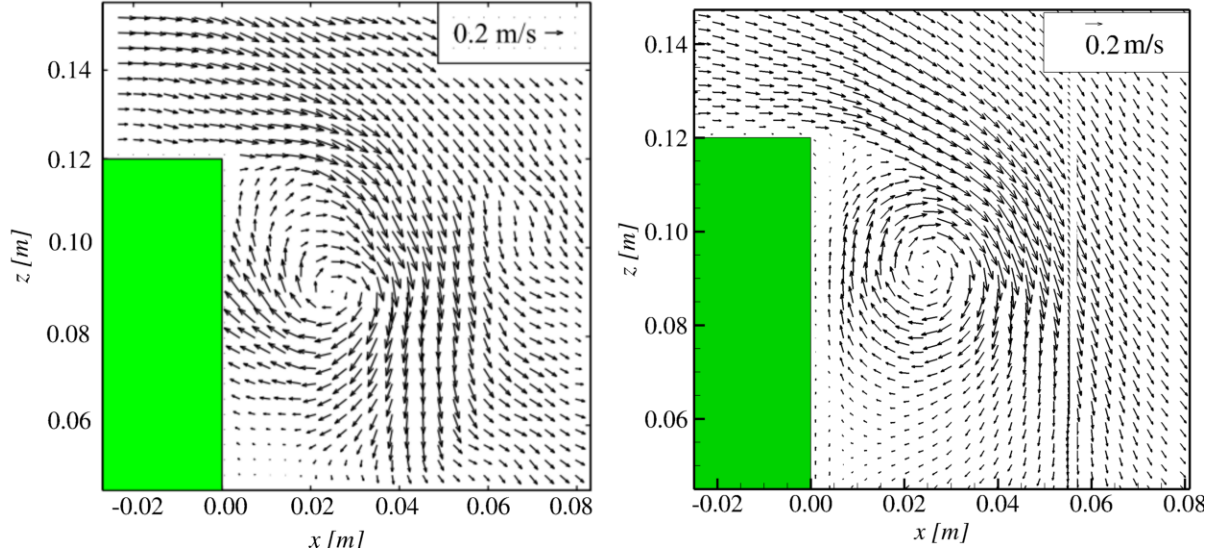
(a) Velocity vectors
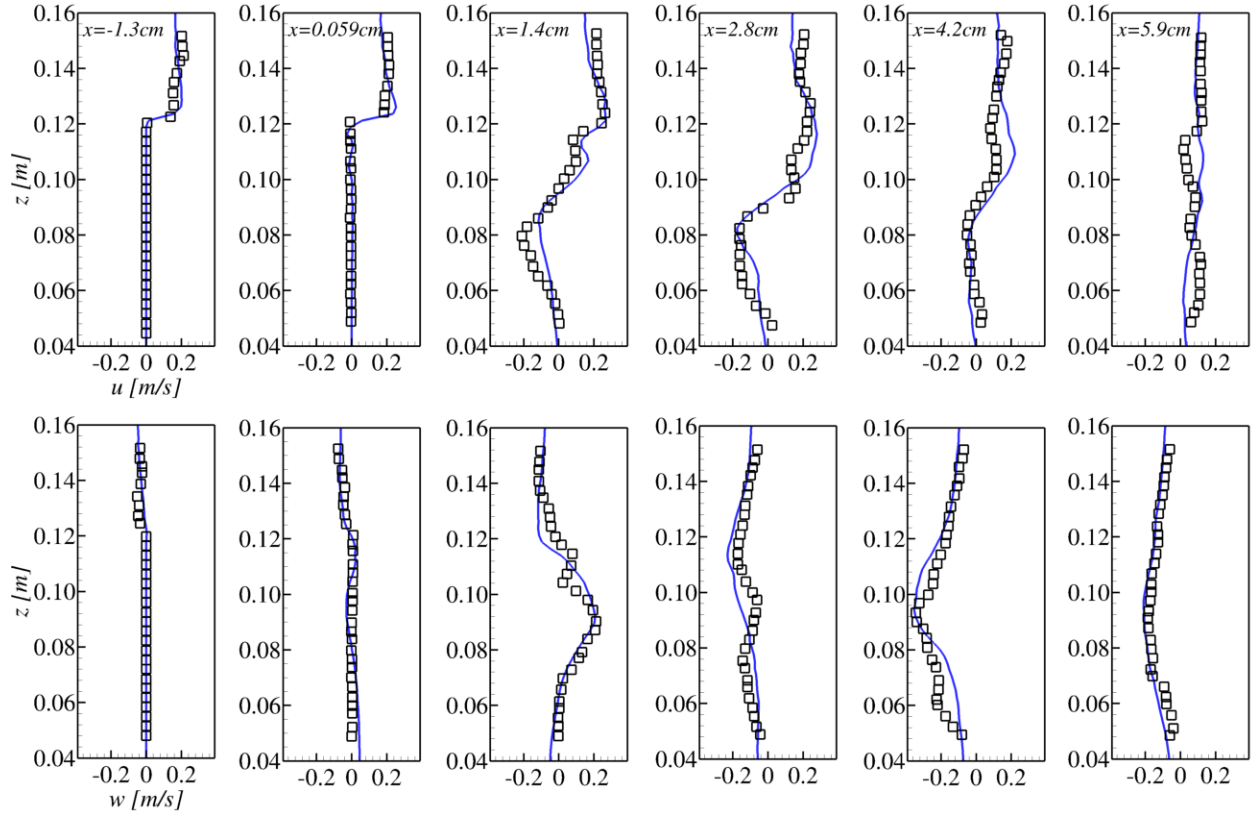
(b) Velocity profiles of the horizontal and vertical velocity components

Fig. 18: (a) Simulated (right) and PIV-measured (left) instantaneous velocity vectors and (b) LES-predicted (solid lines) and measured (open squares) profiles of the the horizontal (upper row) and vertical (lower row) velocities (b) at t=1.2s.

Figure 17a plots the simulated (right panel) and the PIV-measured (left panel) velocity vector field near the trailing edge of the step at $t = 0$ sec. At this instance, the wave trough located above the trailing

edge generates a backflow (from right to left) due to the low hydrostatic pressure below the water surface.

435 This backflow separates from the leading edge of the step and forms a strong eddy with counterclockwise rotation. At about $3cm$ above the step's trailing edge, which is where the eddy is less effective, the back flow is almost uniform over the step. The predictions match well with the laboratory measurements. The shape and intensity of the calculated eddy is very similar to the one observed in the experiments however, its location is slightly shifted towards the trailing edge. A more quantitative assessment of the LES' performance

440 is possible with the help of Figure 17b plotting simulated (solid lines) and measured (open squares) profiles of the horizontal and vertical velocity components at various locations. Simulated velocity profiles agree reasonably well with the data obtained from [53]. Better agreement is observed in the horizontal velocity component but vertical velocities also follow the laboratory results with a sufficient degree of accuracy. At $x = -3.7cm$ the maximum magnitude of the horizontal velocity is calculated at a higher vertical location

445 than what was measured in the experiments and the vertical velocity is slightly underestimated in the simulations at $x = -1.2cm$ and $x = -0.2cm$. Nevertheless, simulations are in a good agreement with the PIV measurements.

Similarly, Fig. 18 presents LES-predicted and measured velocity vectors at $t = 1.2sec$. At this instance, the progression of the wave crest and high hydrostatic pressure, over the step's trailing edge develops a

450 positive flow (from left to right), which separates at the leading edge of the step thereby forming a clockwise-rotating vortex just above the edge. The simulated velocity vectors (right panel) match well the laboratory measurements (left panel) and the location of the eddy is predicted accurately. An almost uniform flow over the step is observed. In Fig. 18b, simulated velocity profiles upstream and downstream of the trailing edge are in a very good agreement with the laboratory measurements. The boundary layers in the horizontal

455 velocity component, at $x = -1.3cm$ and $x = 0.059cm$ are well captured by Hydro3D-NWT, a key-factor for properly reproducing flow separation around the trailing edge. Moreover, the vertical and horizontal velocity profiles follow the experimental measurements with only minor discrepancies at the eddy's location at $2.8cm \leq x \leq 4.2cm$.

In Figs. 19 to 21 the flow field over the leading edge of the submerged step is presented via vectors and

460 examined in more detailed via velocity profiles. The vector field is plotted in Fig. 20 and Fig. 21 at $t = 0.4$ sec and $t = 0.8$ sec , respectively, for both the simulation and the experiment. At $t = 0.4$ sec, Fig. 20a shows a negative flow near the leading edge and the presence of a dominant counter-clockwise-rotating vortex upstream of the structure. The simulated velocity vectors (right panel) are in a very good agreement with the experimental measurements (left panel) and the overall flow and location of the vortex are well

465 captured. In Fig. 20b velocity profiles downstream and upstream of the leading edge follow the data of the PIV measurements and the simulated velocities compare well with [53]. Furthermore, both the velocity magnitude and change in flow direction at the location of the vortex, are well captured. Figure 21 presents velocity vectors at $t = 0.8$ sec at which the crest of the wave approaches the leading edge. In Fig. 21a a positive flow develops, separating at the leading edge of the step and a small clockwise-rotating vortex is

31

formed just above the step corner. Simulated velocity vectors (right panel) show that the location of the
eddy is in agreement with experiments (left panel) however the height of the eddy is slightly overestimated by
Hydro3D-NWT. Due to this, the simulated velocity profiles in Fig. 21b are inconsistent with the experiments,
mostly near the step's top boundary (at $z \leq 0.14$) where the vortex is located whereas further downstream,
simulations well capture the velocity field.

Figure 22 visualises the formation of eddies near the submerged step using iso-surfaces of Q-criterion at
$Q = 60$ coloured with the Y-vorticity. In Fig. 22a, the formation of eddies near the trailing edge of the
step is presented at $t = 1.2$ sec (corresponding to (2) in Fig. 16). An energetic vortex extending in the
spanwise direction almost over the entire trailing edge is observed. Most interesting is the slight meandering
of the eddy, i.e. not perfectly two dimensional, suggesting the presence of minor 3D instabilities. These
are noticed as smaller billows (with zero y-vorticity) in the vicinity of the main vortex. Also at various
locations along the spanwise direction secondary spanwise vortices, contoured in red, are observed, which
are counter-rotating to the main separated vortex, coloured mainly in blue. The leading edge vortex at
$t = 0.4$ sec (corresponding to (1) in Fig. 19) is visualised in Fig. 22b provide further evidence of the slight
three-dimensionality of this flow. The spanwise vortex is broken up at various locations near the leading
edge, and minor secondary counter-rotating vortices are observed. Obviously, the relatively narrow tank, the
quasi-two-dimensional waves and the step geometry promote 2-dimensional flow structures, however it won't
take a lot of variation in either of these parameters before significant 3D-wave-structure-interaction takes
place, which Hydro3D-NWT is able to resolve accurately. The results suggest that large eddy simulations
executed on a relatively fine mesh are capable of predicting complex WSI.
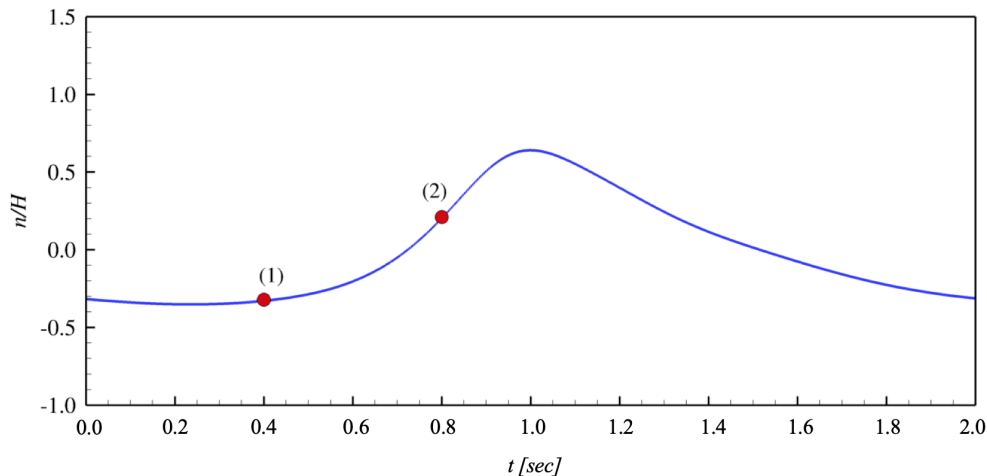
Fig. 19: Wave above the leading edge of the step. Markers (1) and (2) represents the time steps at which velocity vectors and
local velocity profiles are plotted in Fig. 20 and Fig. 21, respectively.
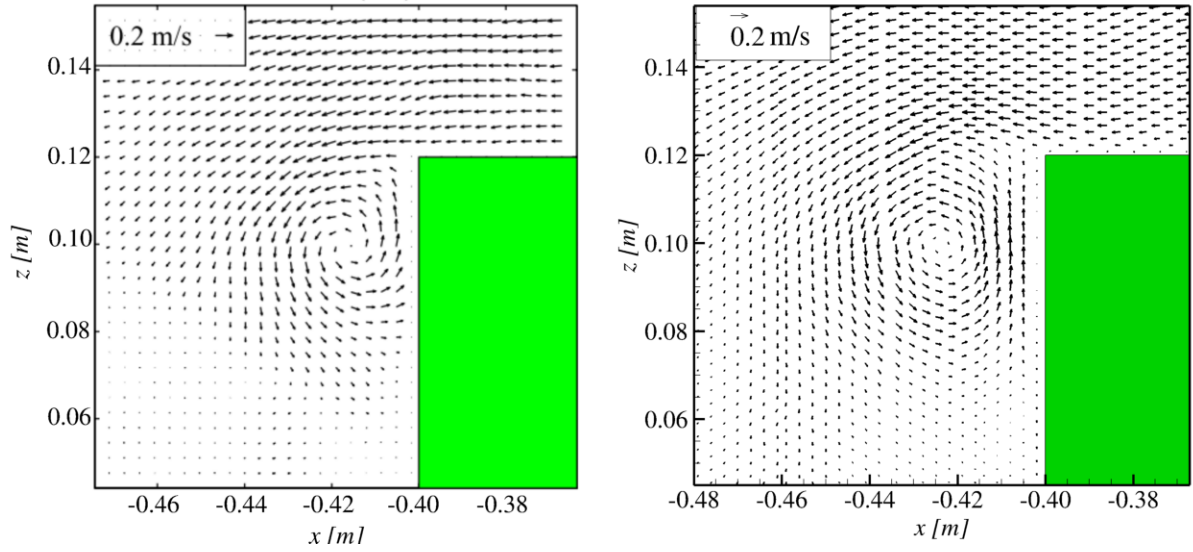
(a) Velocity vectors
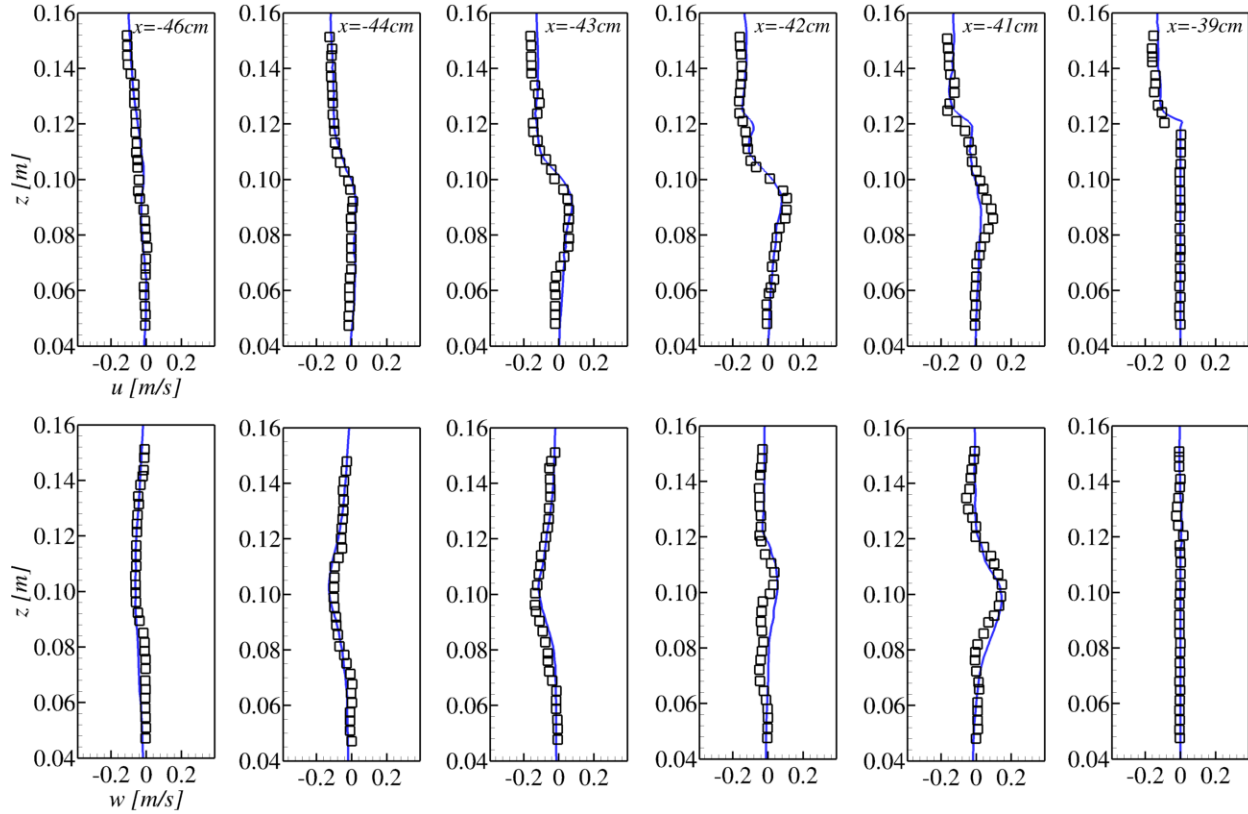
(b) Velocity profiles of the horizontal and vertical velocity components

Fig. 20: (a) Simulated (right) and PIV-measured (left) instantaneous velocity vectors near the leading edge and (b) LES-predicted (solid lines) and measured (open squares) profiles of the the horizontal (upper row) and vertical (lower row) velocities (b) at t=0.4s.
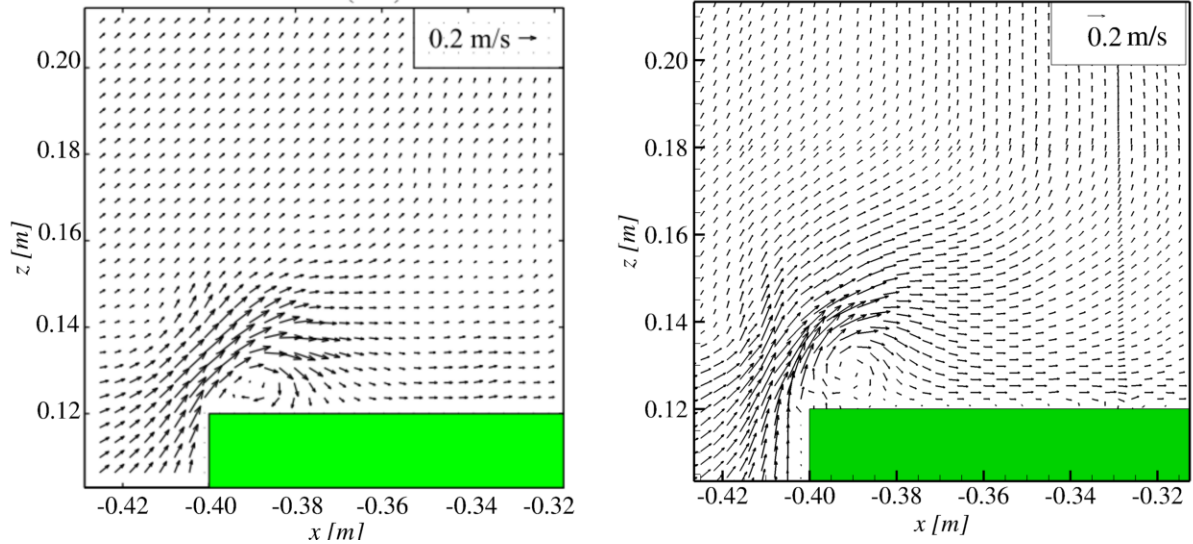
33
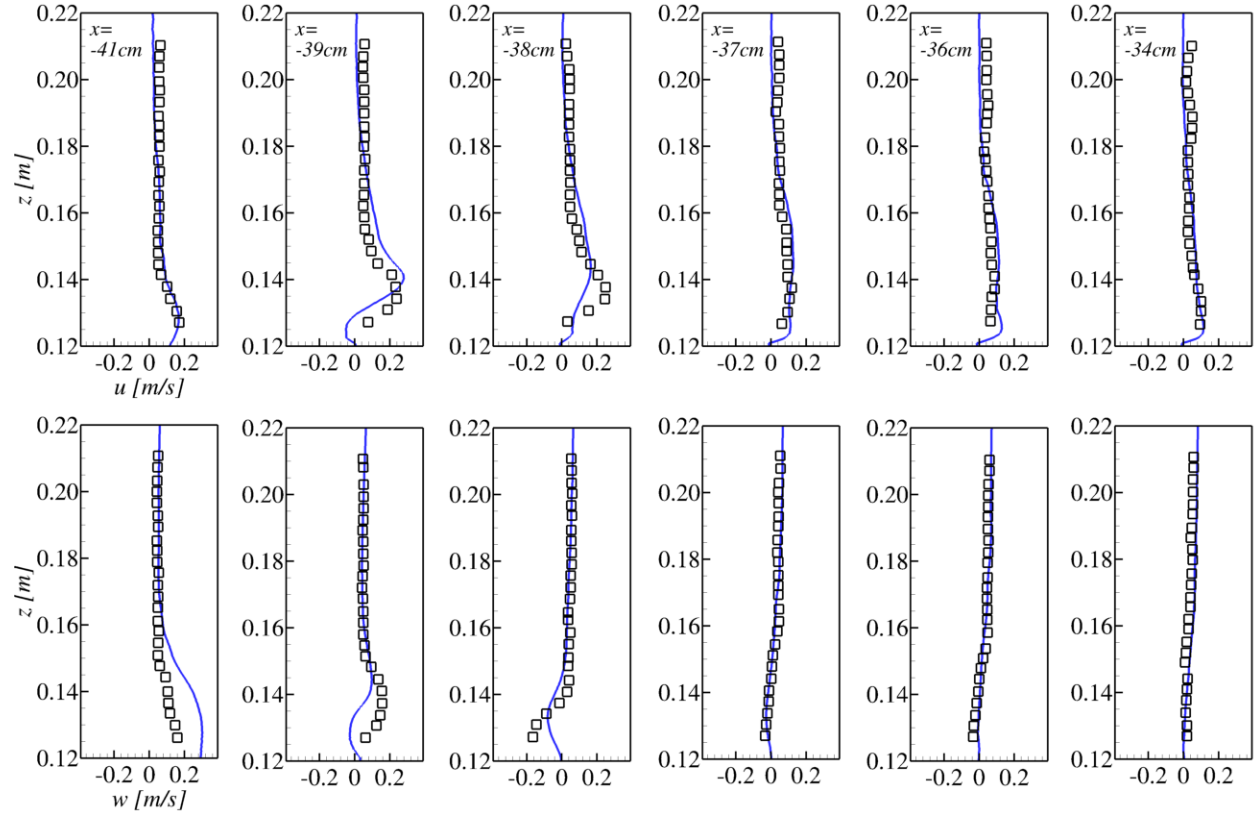
(a) Velocity vectors

(b) Velocity profiles of the horizontal and vertical velocity components

Fig. 21: (a) Simulated (right) and PIV-measured (left) instantaneous velocity vectors near the leading edge and (b) LES-predicted (solid lines) and measured (open squares) profiles of the the horizontal (upper row) and vertical (lower row) velocities (b) at t=0.8s.

(a) Y-vorticity near trailing edge

(b) Y-vorticity near leading edge
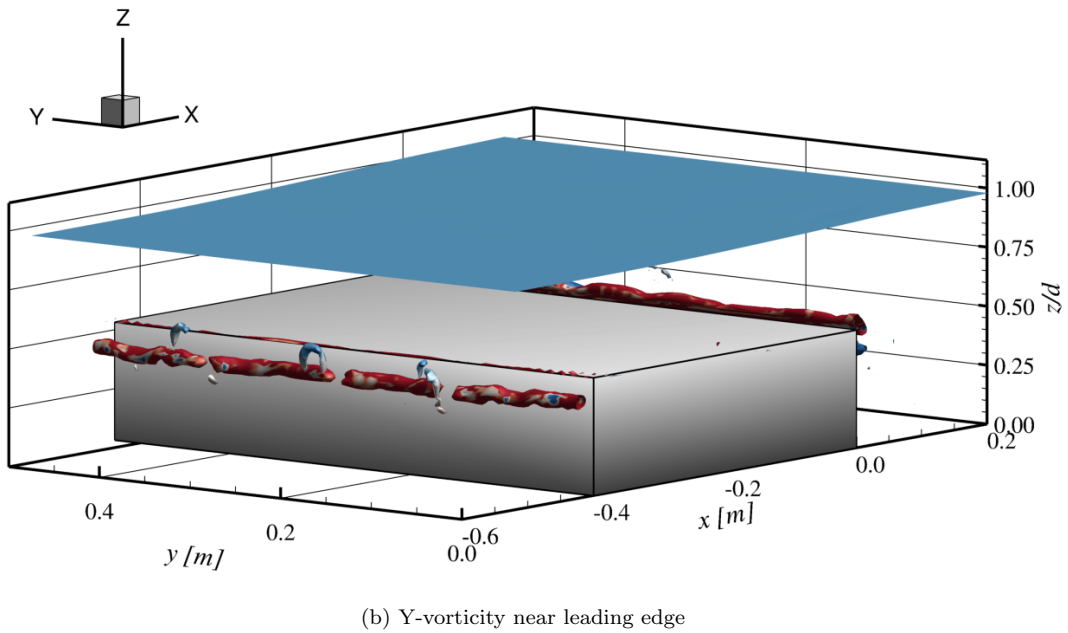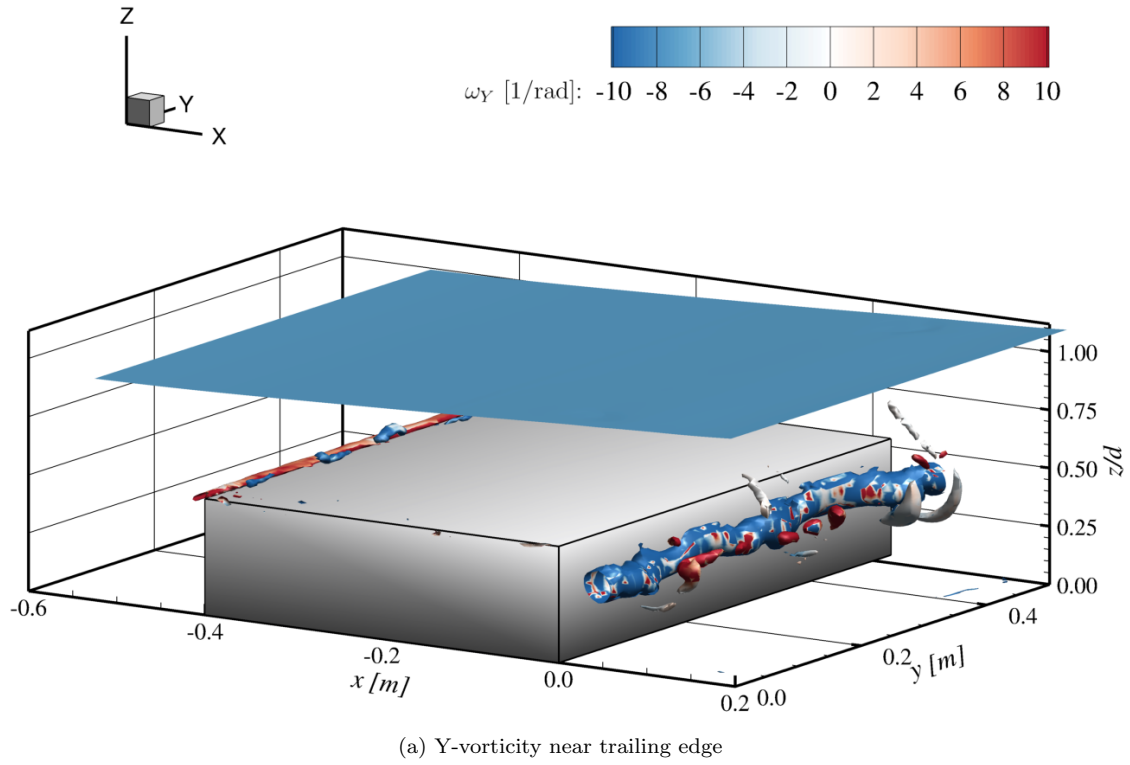
Fig. 22: Plots of the iso-surface of $\phi = 0$ and Q-criterion$= 60$ coloured by Y-vorticity, (a) near the trailing at $t = 1.2$ sec (marker 2 in Fig. 16) and (b) at leading edge at $t = 0.4$ sec (marker 1 in Fig. 19).

35

3.3. Wave-plate interaction

(a) top view
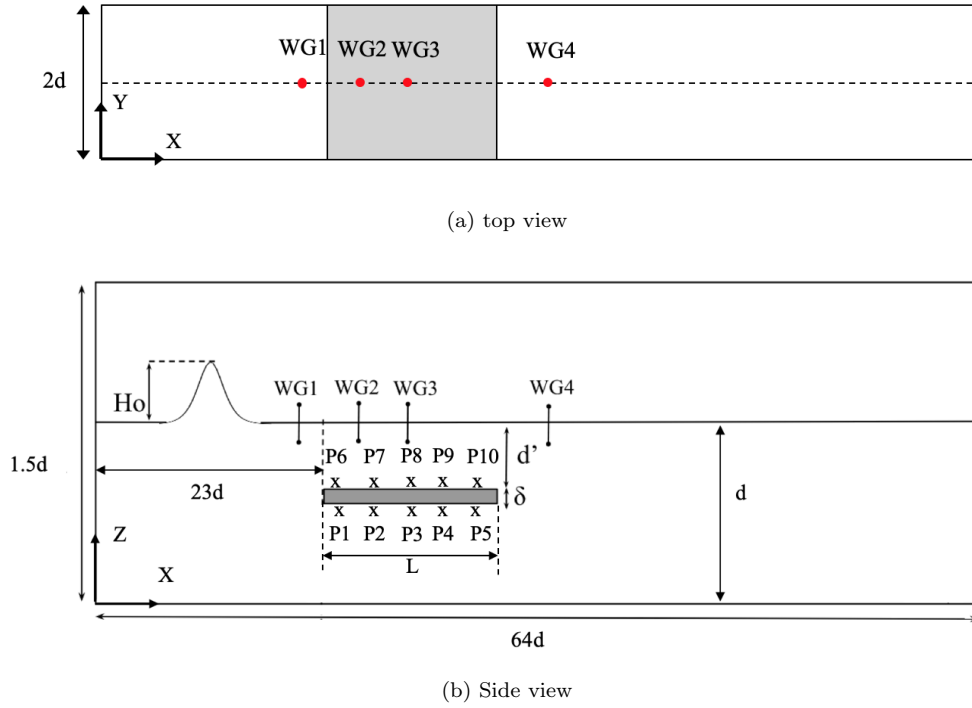
(b) Side view

Fig. 23: Schematic diagram of a submerged plate under the action of a solitary wave. (a) top view, (b) side view.

In this section, a laboratory experiment previously conducted by [1] of a solitary wave propagating over a flat plate is reproduced by Hydro3D-NWT. Figure 23 sketches a $L = 1.156m$ long plate of thickness $\delta = 0.01m$, submerged halfway through the tank at still water depth of $d'/d = 0.5$ where d' is the plate's submergence (measured from still water level to the plate's upper surface) and $d = 0.2m$ is the still water depth. The structure is located $23d$ from the wave maker and extends in spanwise throughout the numerical tank. The NWT is $64d$ long, $2d$ wide and $1.5d$ tall and discretised with $2560 \times 80 \times 120$ ($N_x \times N_y \times N_z$) equally sized cells which gives mesh spacings of $dx/d = dy/d = 0.025$, $dz/d = 0.0125$. A fixed time step of $dt = 0.001$ sec is adopted throughout the simulation. Four wave gauges are distributed over the centreline of the tank to capture the wave's propagation through the tank and ten pressure sensors are fixed around the structure (cross symbols in Fig. 23) to record the pressure acting on the plate. The exact location of pressure sensors and wave gauges are shown in Table 3 and Table 4, respectively. In [1] various submergence depths and wave heights were tested, in the simulations a wave height of $H_0/d = 0.1$, a wavelength of $\lambda/d = 22.945$ and an effective wave period of $T = 3.123$ sec are adopted and prescribed using analytical solutions of wave elevation and water velocities based on Boussinesq theory [55].

Table 3: Pressure-sensors' locations.

Sensor	Location (m)
P1, P6	0.1
P2, P7	0.35
P3, P8	$L/2$
P4, P9	$L - 0.35$
P5, P10	$L - 0.1$

Table 4: Wave-gauges' locations.

Gauge	Location (m)
WG1	$-\lambda/4$
WG2	0.1
WG3	$L/2$
WG4	$L + \lambda/4$

Dirichlet boundary conditions for the water surface and velocity components are applied at the inlet of the NWT, whereas periodic boundary conditions are set at the south and north boundaries. A Neumann boundary condition for the pressure at all boundaries and a no-slip condition for the bottom of the tank and the plate's surfaces are employed. The top boundary of the tank is treated as a free-slip boundary. In the following figures, water levels, force and moments acting on the plate as well as a time series of the non-hydrostatic pressure are presented and comparisons are made with the experimental data of [1]. It is noted here that in all calculations, hydrostatic pressure due to the still water level ($\rho g(d - z)$) is ignored in order to be consistent with the experimental data.

Figure 24 plots computed wave elevations (solid lines) as recorded at WG1-WG4 together with experimental data (open squares). The computed water levels agree well with the laboratory measurements at all wave-gauges. At WG1, the initial wave height is properly captured and subsequent wave reflections or harmonics due to the impact of the wave with the submerged plate are well predicted. The simulated wave elevations captured by WG2 and WG3 follow the experiments and a slight increase in wave height is observed due to shallowness of the water above the structure and the developing boundary layer above the plate, which leads to wave steepening. At WG4, a drop in wave height is found, the result of energy dissipation due to friction of the plate, however the result is slightly overestimated in the simulations compared to the experiment.

Figure 25 presents the vertical force (F_z) and the corresponding moment (M_c) measured about the center of the plate to further examine the performance of Hydro3D-NWT. The predicted pressure is integrated over the top and bottom surfaces of the plate to obtained the force and the moment, which are normalized with $F_0 = \rho g H_0 L$ and $M_0 = F_0 L/2$, respectively. In Fig. 25a, the predicted vertical force (solid lines) and the experimental data (open squares) are plotted. The simulated vertical force is in good agreement with the experimental data and the vertical force acting on the plate as a function of time is captured well. When the wave is closed to the plate's leading edge, a uniform flow below the structure is observed, compared to an almost stationary flow above, that generates a higher pressure and thus a positive, upward force acting on the plate (at $t'/T = -0.1$). Once the wave is over the plate (at $t'/T = 0.15$), a downward force due to the weight of the wave is recorded followed by a secondary positive force. The calculated moment on the plate
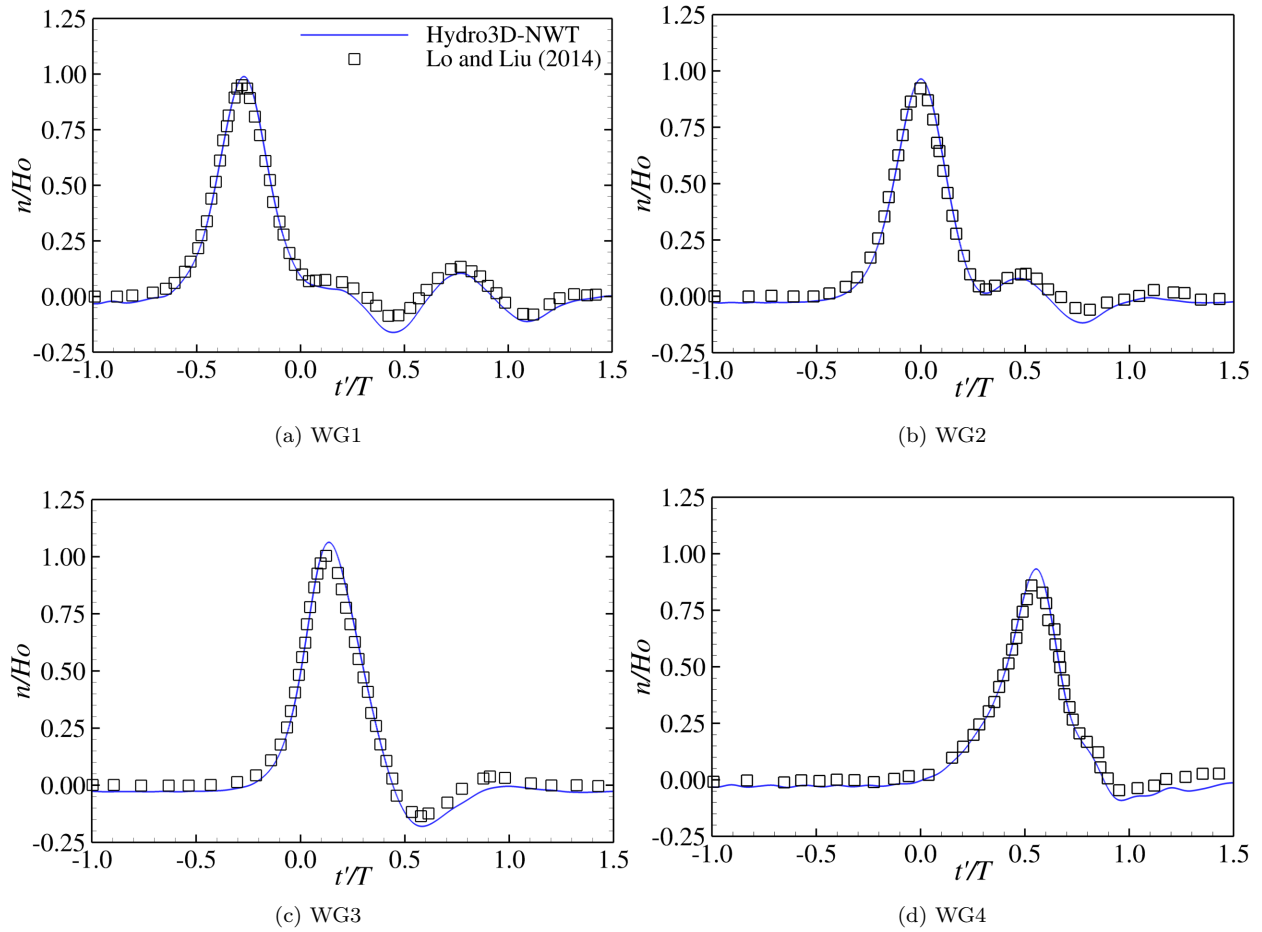
Fig. 24: Simulated water surface elevations (solid lines) and experimental data of [1] (open squares) at (a) WG1 (b) WG2 (c) WG3 and (d) WG4.

as plotted in Fig. 25b does not agree very well with the experimental measurement. This was also found by [56] and [1] and this might be the result of the relatively coarse spatial resolution of the pressure sensors in the laboratory study.

Figure 26 describes the time history of the local pressure over the plate as the wave propagates through the tank. $P1 - P5$ are located under the plate while $P6 - P10$ are on the top of the plate. The simulated normalised pressure (solid lines) is plotted together with experimental data (open squares) and very good agreement is achieved. Overall, the simulations follow the laboratory measurements in all locations however, some slight overpredictions of the peaks of the non-hydrostatic pressure are observed. These are mainly on the underside of the plate and towards the trailing edge (P4 and P5) whereas for the locations on the top of the structure Hydro3D-NWT returns very good results. This might be due to the complex flow near the plate's edges, i.e. the interaction of trailing edge vortices with the plate, which would probably need a higher spatial resolution in this area. However it may also be experimental uncertainty.

(a) Vertical force (F_z)
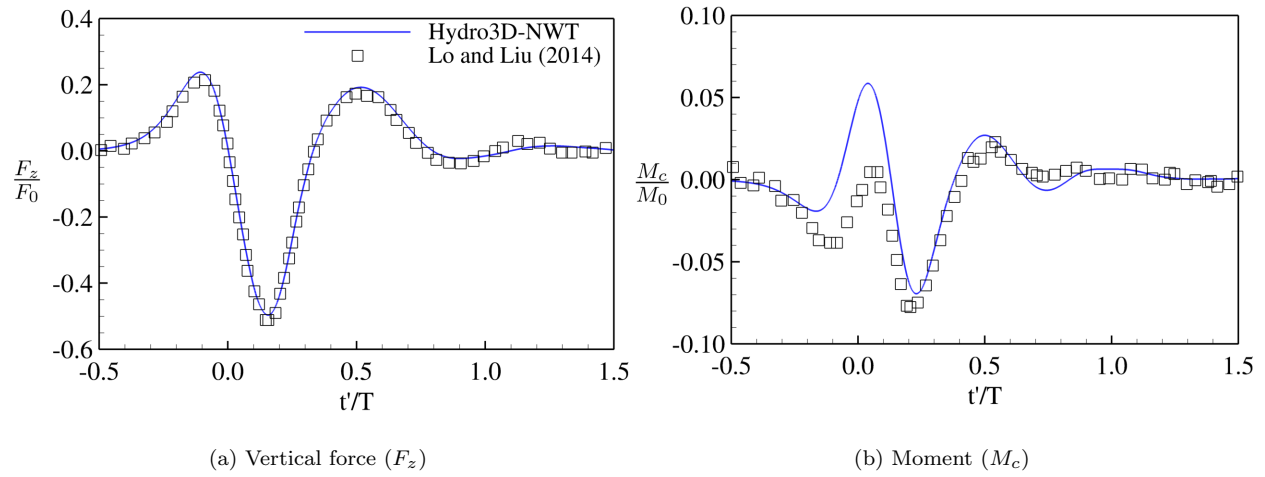
(b) Moment (M_c)

Fig. 25: Simulated (solid lines) and measured [1] (a) vertical force (F_z/F_0) on the plate and (b) moment about the centre of the plate (M_c/M_0).
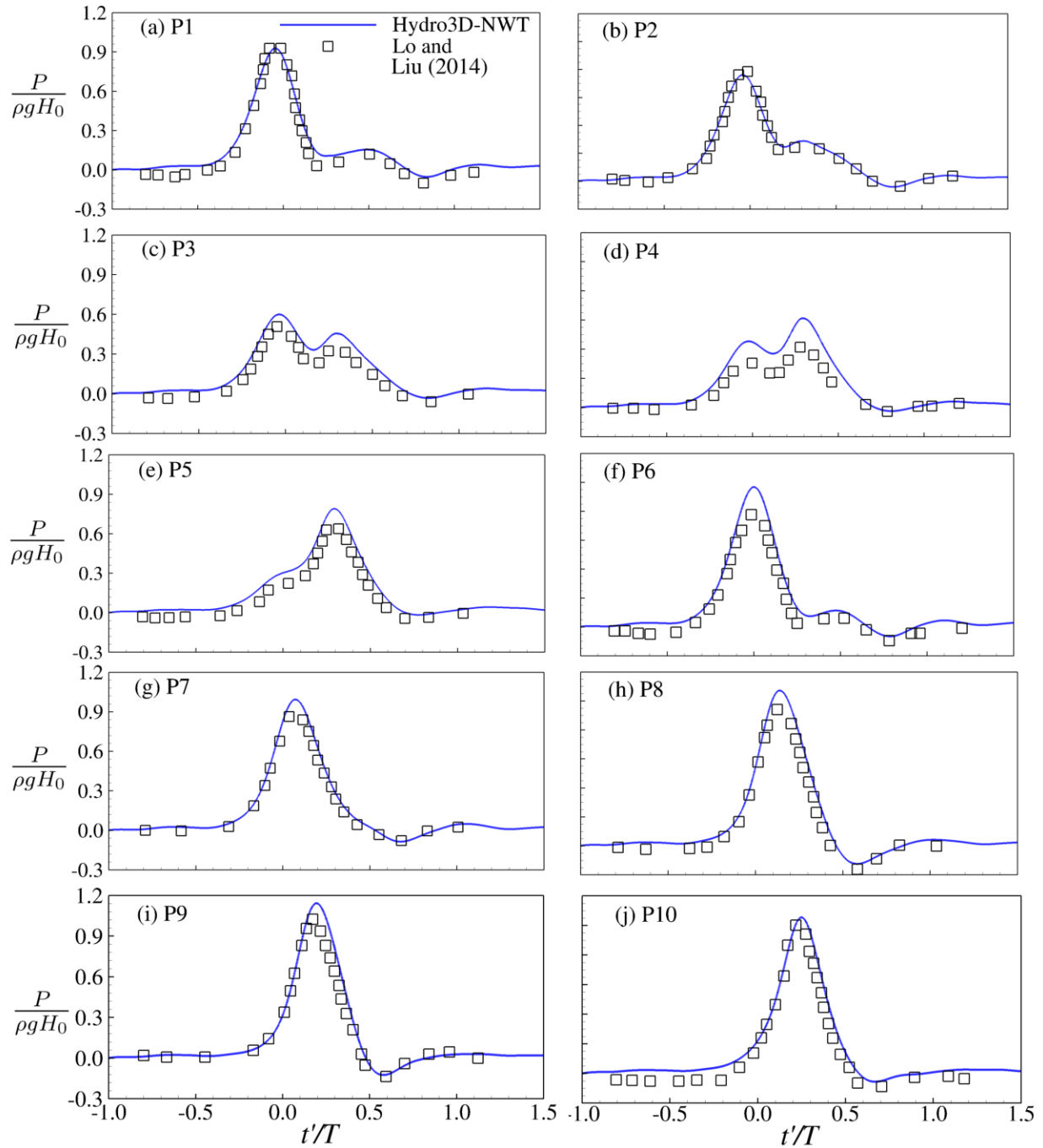
Fig. 26: Predicted (solid lines) non-hydrostatic pressure $\frac{P}{\rho g H_0}$ together with experimental data [1] (open squares) at (a) P1 - (j) P10 locations.

4. Conclusions

545   An open-source large-eddy-simulation-based numerical wave tank, Hydro3D-NWT, has been introduced and described in detail. The code solves the filtered Navier-Stokes equations and features a novel combination of immersed boundary and level set methods which allows investigating realistic and three-dimensional

wave-offshore-structure-interaction. The results of several simulations have been presented with the goal to showcase the validity, credibility and accuracy of Hydro3D-NWT. First, the run-up of a solitary wave on a vertical wall is simulated with the goal to verify the free-surface capturing technique and the results suggest that Hydro3D-NWT captures the propagation and run-up precisely. Then two types of wave propagation through a tank, without any structure, are simulated and results of wave elevations, viscous damping and local velocity field are convincingly accurate. After that, Hydro3D-NWT has been applied to rather complex WSI problems of coastal and offshore engineering interest. Simulations of 2nd order Stokes, cnoidal and solitary waves interacting with submerged structures, including a rectangular step, a trapezoidal bar and a thin, submerged plate, have been performed. The results have been compared with experimental measurements of free-surface elevations, water velocities as well as hydrodynamic forces, pressure on the structures and moments. Comparisons of HYdro3D-NWT-predicted results with experimental data evidence that Hydro3D-NWT is able to return convincing agreement, in particular for WSI problems in which three-dimensional and viscous effects, albeit small for the three cases shown here, play a role. The current study suggest that Hydro3D-NWT can be a reliable tool for simulating complex 3D WSI problems and additional simulations are to be conducted in the near future to investigate WSI problems with dominant three-dimensional effects for fixed and floating structures.

5. Acknowledgements

References

[1] Lo, H.Y., Liu, P.L.. Solitary waves incident on a submerged horizontal plate. Journal of Waterway, Port, Coastal and Ocean Engineering 2014;140(3):1–17. doi:10.1061/(ASCE)WW.1943-5460.0000236.

[2] Pawitan, K.A., Dimakopoulos, A.S., Vicinanza, D., Allsop, W., Bruce, T.. A loading model for an OWC caisson based upon large-scale measurements. Coastal Engineering 2019;145:1–20. doi:10.1016/j.coastaleng.2018.12.004.

[3] Esandi, J.M., Buldakov, E., Simons, R., Stagonas, D.. An experimental study on wave forces on a vertical cylinder due to spilling breaking and near-breaking wave groups. Coastal Engineering 2020;162:103778. doi:10.1016/j.coastaleng.2020.103778.

[4] Shao, Y.L., Faltinsen, O.M.. A harmonic polynomial cell (HPC) method for 3D Laplace equation with application in marine hydrodynamics. Journal of Computational Physics 2014;274:312–332. doi:10.1016/j.jcp.2014.06.021.

[5] Ducrozet, G., Engsig-Karup, A.P., Bingham, H.B., Ferrant, P.. A non-linear wave decomposition model for efficient wave-structure interaction. Part A: Formulation, validations and analysis. Journal of Computational Physics 2014;257:863–883. doi:10.1016/j.jcp.2013.09.017.

[6] Onguet-Hig, M.S.L., Cokelet, E.D.. The deformation of steep surface waves on water - I. A numerical method of computation. Proceedings of the Royal Society of London A Mathematical and Physical Sciences 1976;350(1660):1–26. doi:10.1098/rspa.1976.0092.

[7] Liu, C., Huang, Z., Keat Tan, S.. Nonlinear scattering of non-breaking waves by a submerged horizontal plate: Experiments and simulations. Ocean Engineering 2009;36(17-18):1332–1345. doi:10.1016/j.oceaneng.2009.09.001.

[8] Hayatdavoodi, M., Ertekin, R.C.. Wave forces on a submerged horizontal plate - Part I: Theory and modelling. Journal of Fluids and Structures 2015;54:566–579. doi:10.1016/j.jfluidstructs.2014.12.010.

[9] Hayatdavoodi, M., Ertekin, R.C.. Wave forces on a submerged horizontal plate-Part II: Solitary and cnoidal waves. Journal of Fluids and Structures 2015;54:580–596. doi:10.1016/j.jfluidstructs.2014.12.009.

[10] Green, A.E., Naghdi, P.M.. Water waves in a nonhomogeneous incompressible fluid. Journal of Applied Mechanics, Transactions ASME 1977;44(4):523–528. doi:10.1115/1.3424129.

[11] Smagorisnky, J.. General circulation experiments with the primitive equations. Monthly Weather Review 1963;91(3):99–164. doi:10.1175/1520-0493(1963)091<0099:gcewtp>2.3.co;2.

[12] Nicoud, F., Ducros, F.. Subgrid-scale stress modelling based on the square of the velocity gradient tensor. Flow, Turbulence and Combustion 1999;62(3):183–200. doi:10.1023/A:1009995426001.

[13] Stoesser, T.. Large-eddy simulation in hydraulics: Quo Vadis? Journal of Hydraulic Research 2014;52(4):441–452. doi:10.1080/00221686.2014.944227.

[14] Osher, S., Sethian, J.A.. Fronts propagating with curvature-dependent speed: Algorithms based on Hamilton-Jacobi formulations. Journal of Computational Physics 1988;79(1):12–49. doi:10.1016/0021-9991(88)90002-2.

[15] Hirt, C.W., Nichols, B.D.. Volume of fluid (VOF) method for the dynamics of free boundaries. Journal of Computational Physics 1981;39(1):201–225. doi:10.1016/0021-9991(81)90145-5.

[16] Shu, C.W.. High Order Weighted Essentially Nonoscillatory Schemes for Convection Dominated Problems. SIAM Review 2009;51(1):82–126. doi:10.1137/070679065.

[17] McSherry, R.J., Chua, K.V., Stoesser, T.. Large eddy simulation of free-surface flows. Journal of Hydrodynamics 2017;29(1):1–12. doi:10.1016/S1001-6058(16)60712-6.

[18] Wang, Z., Yang, J., Koo, B., Stern, F.. A coupled level set and volume-of-fluid method for sharp interface simulation of plunging breaking waves. International Journal of Multiphase Flow 2009;35(3):227–246. doi:10.1016/j.ijmultiphaseflow.2008.11.004.

[19] Higuera, P., Lara, J.L., Losada, I.J.. Realistic wave generation and active wave absorption for Navier-Stokes models. Application to OpenFOAM®. Coastal Engineering 2013;71:102–118. URL: http://dx.doi.org/10.1016/j.coastaleng.2012.07.002. doi:10.1016/j.coastaleng.2012.07.002.

[20] Jacobsen, N.G., Fuhrman, D.R., Fredsøe, J.. A wave generation toolbox for the open-source CFD library: OpenFoam®. International Journal for Numerical Methods in Fluids 2012;70(9):1073–1088. URL: http://doi.wiley.com/10.1002/fld.2726. doi:10.1002/fld.2726.

[21] Higuera, P., Losada, I.J., Lara, J.L.. Three-dimensional numerical wave generation with moving boundaries. Coastal Engineering 2015;101:35–47. doi:10.1016/j.coastaleng.2015.04.003.

[22] Mayer, S., Garapon, A., Sørensen, L.S.. A fractional step method for unsteady free-surface flow with applications to non-linear wave dynamics. International Journal for Numerical Methods in Fluids 1998;28(2):293–315. doi:10.1002/(SICI)1097-0363(19980815)28:2<293::AID-FLD719>3.0.CO;2-1.

[23] Xie, Z., Stoesser, T., Yan, S., Ma, Q., Lin, P.. A Cartesian cut-cell based multiphase flow model for large-eddy simulation of three-dimensional wave-structure interaction. Computers & Fluids 2020;213:104747. URL: https://linkinghub.elsevier.com/retrieve/pii/S0045793020303170. doi:10.1016/j.compfluid.2020.104747.

[24] Xie, Z., Stoesser, T.. A three-dimensional Cartesian cut-cell/volume-of-fluid method for two-phase flows with moving bodies. Journal of Computational Physics 2020;416:109536. URL: www.elsevier.com/locate/jcp. doi:10.1016/j.jcp.2020.109536.

[25] Bihs, H., Kamath, A., Alagan Chella, M., Aggarwal, A., Arntsen, Ø.A.. A new level set numerical wave tank with improved density interpolation for complex wave hydrodynamics. Computers and Fluids 2016;140:191–208. doi:10.1016/j.compfluid.2016.09.012.

[26] Alagan Chella, M., Bihs, H., Myrhaug, D., Muskulus, M.. Breaking characteristics and geometric properties of spilling breakers over slopes. Coastal Engineering 2015;95:4–19. doi:10.1016/j.coastaleng.2014.09.003.

[27] Berthelsen, P.A., Faltinsen, O.M.. A local directional ghost cell approach for incompressible viscous flow problems with irregular boundaries. Journal of Computational Physics 2008;227(9):4354–4397. doi:10.1016/j.jcp.2007.12.022.

[28] Frantzis, C., Grigoriadis, D.G.. An efficient method for two-fluid incompressible flows appropriate for the immersed boundary method. Journal of Computational Physics 2019;376:28–53. doi:10.1016/j.jcp.2018.09.035.

[29] Frantzis, C., Grigoriadis, D.G., Dimas, A.A.. An efficient Navier-Stokes based numerical wave tank using fast Poisson solvers and the immersed boundary method. Ocean Engineering 2020;196. doi:10.1016/j.oceaneng.2019.106832.

[30] Uhlmann, M.. An immersed boundary method with direct forcing for the simulation of particulate flows. Journal of Computational Physics 2005;209(2):448–476. doi:10.1016/j.jcp.2005.03.017.

[31] Calderer, A., Guo, X., Shen, L., Sotiropoulos, F.. Fluid–structure interaction simulation of floating structures interacting with complex, large-scale ocean waves and atmospheric turbulence with application to floating offshore wind turbines. Journal of Computational Physics 2018;355:144–175. doi:10.1016/j.jcp.2017.11.006.

[32] GitHub - OuroPablo/Hydro3D: Hydro3D - Official repository. 2020. URL: https://github.com/OuroPablo/Hydro3D.

[33] Stoesser, T., McSherry, R., Fraga, B.. Secondary Currents and Turbulence over a Non-Uniformly Roughened Open-Channel Bed. Water 2015;7(12):4896–4913. doi:10.3390/w7094896.

[34] Cevheri, M., McSherry, R., Stoesser, T.. A local mesh refinement approach for large-eddy simulations of turbulent flows. International Journal for Numerical Methods in Fluids 2016;82(5):261–285. doi:10.1002/fld.4217.

[35] Fraga, B., Stoesser, T., Lai, C.C., Socolofsky, S.A.. A LES-based Eulerian-Lagrangian approach to predict the dynamics of bubble plumes. Ocean Modelling 2016;97:27–36. doi:10.1016/j.ocemod.2015.11.005.

[36] Christou, A., Xie, Z., Stoesser, T., Ouro, P.. Propagation of a solitary wave over a finite submerged thin plate. Applied Ocean Research 2021;106:102425. doi:10.1016/j.apor.2020.102425.

[37] Ouro, P., Fraga, B., Lopez-Novoa, U., Stoesser, T.. Scalability of an Eulerian-Lagrangian large-eddy simulation solver with hybrid MPI/OpenMP parallelisation. Computers and Fluids 2019;179:123–136. doi:10.1016/j.compfluid.2018.10.013.

[38] Chorin, A.J.. Numerical solution of the Navier-Stokes equations. Mathematics of Computation 1968;22(104):745–745. doi:10.1090/S0025-5718-1968-0242392-2.

[39] Ferziger, J.H., Perić, M.. Computational Methods for Fluid Dynamics. Springer Berlin Heidelberg; 2002. doi:10.1007/978-3-642-56026-2.

[40] Roma, A.M., Peskin, C.S., Berger, M.J.. An Adaptive Version of the Immersed Boundary Method. Journal of Computational Physics 1999;153(2):509–534. doi:10.1006/jcph.1999.6293.

[41] Kara, M., Stoesser, T., McSherry, R.. Calculation of fluid structure interaction: methods, refinements, applications. Proceedings of the Institution of Civil Engineers - Engineering and Computational Mechanics 2015;168(2):59–78. doi:10.1680/eacm.15.00010.

[42] Ouro, P., Stoesser, T.. An immersed boundary-based large-eddy simulation approach to predict the performance of vertical axis tidal turbines. Computers and Fluids 2017;152:74–87. doi:10.1016/j.compfluid.2017.04.003.

[43] Kara, S., Kara, M.C., Stoesser, T., Sturm, T.W.. Free-surface versus rigid-lid LES computations for bridge-abutment flow. Journal of Hydraulic Engineering 2015;141(9):1–9. doi:10.1061/(ASCE)HY.1943-7900.0001028.

[44] Kara, S., Stoesser, T., Sturm, T.W., Mulahasan, S.. Flow dynamics through a submerged bridge opening with overtopping. Journal of Hydraulic Research 2015;53(2):186–195. doi:10.1080/00221686.2014.967821.

[45] McSherry, R., Chua, K., Stoesser, T., Mulahasan, S., Mcsherry, R., Associate, R.. Free surface flow over square bars at intermediate relative submergence. Journal of Hydraulic Research 2018;56(6):825–843. doi:10.1080/00221686.2017.1413601.

[46] M. Sussman, P. Smereka, S.O.. A level set approach for computing solutions to incompressible two-phase flow. Journal of Computational Physics 1994;114(1):146–159. doi:10.1006/jcph.1994.1155.

[47] Yue, W., Lin, C.L., Patel, V.C.. Numerical simulation of unsteady multidimensional free surface motions by level set method. International Journal for Numerical Methods in Fluids 2003;42(8):853–884. doi:10.1002/fld.555.

[48] Chan, R.K., Street, R.L.. A computer study of finite-amplitude water waves. Journal of Computational Physics 1970;6(1):68–94. doi:10.1016/0021-9991(70)90005-7.

[49] Mei, C.C.. The applied dynamics of ocean surface waves. John Wiley & Sons; 1983. ISBN 0471064076. doi:10.1016/0029-8018(84)90033-7.

[50] Choi, J., Yoon, S.B.. Numerical simulations using momentum source wave-maker applied to RANS equation model. Coastal Engineering 2009;56(10):1043–1060. doi:10.1016/j.coastaleng.2009.06.009.

[51] Beji, S., Battjes, J.A.. Experimental investigation of wave propagation over a bar. Coastal Engineering 1993;19(1-2):151–162. doi:10.1016/0378-3839(93)90022-Z.

[52] Beji, S., Battjes, J.A.. Numerical simulation of nonlinear wave propagation over a bar. Coastal Engineering 1994;23(1-2):1–16. doi:10.1016/0378-3839(94)90012-4.

[53] Chang, K.A., Hsu, T.J., Liu, P.L.. Vortex generation and evolution in water waves propagating over a submerged rectangular obstacle. Part II: Cnoidal waves. Coastal Engineering 2005;52(3):257–283. doi:10.1016/j.coastaleng.2004.11.006.

[54] Wiegel, R.L.. A presentation of cnoidal wave theory for practical application. Journal of Fluid Mechanics 1960;7(2):273–286. URL: https://doi.org/10.1017/S0022112060001481. doi:10.1017/S0022112060001481.

[55] Lee, J.J., Skjelbreia, E., Raichlen, F.. Measurement of velocities in solitary waves. Journal of Waterway, Port, Coastal, and Ocean Engineering 1982;108:200–218.

[56] Ai, C., Ma, Y., Yuan, C., Dong, G.. Semi-implicit non-hydrostatic model for 2D nonlinear wave interaction with a floating/suspended structure. European Journal of Mechanics, B/Fluids 2018;72:545–560. doi:10.1016/j.euromechflu.2018.08.003.